

Simulated reflectance above snow, constrained by airborne measurements of solar radiation: Implications for the snow grain morphology in the Arctic

Soheila Jafariserajehlou^{1, a}, Vladimir V. Rozanov¹, Marco Vountas¹, Charles K. Gatebe^{2,3} and John P. Burrows¹

¹Institute of Environmental Physics, University of Bremen, Bremen, Germany

²Universities Space Research Association (USRA), Columbia, MD, USA

³NASA Goddard Space Flight Center, Greenbelt, MD, USA

^a now at European Organisation for the Exploitation of Meteorological Satellites, Darmstadt, Germany and Rhea System GmbH, Darmstadt, Germany

Correspondence to: Soheila Jafariserajehlou (jafari@iup.physik.uni-bremen.de)

Abstract. Accurate knowledge of the reflectance from snow/ice covered surface is of fundamental importance for the retrieval of snow parameters and atmospheric constituents from space-based and airborne observations.

In this paper, we simulate the reflectance in a snow-atmosphere system using the phenomenological radiative transfer model SCIATRAN and compare the results with that of airborne measurements. To minimize the differences between measurements and simulation, we determine and employ the key atmospheric and surface parameters such as snow grain morphologies (or habits).

Firstly, we report on a sensitivity study. This addresses the requirement for adequate a priori knowledge about snow models and ancillary information about the atmosphere. For this aim, we use the well-validated phenomenological radiative transfer model SCIATRAN. Secondly, we present and apply a two-stage snow grain morphology (i.e. size and shape of ice crystals in the snow) retrieval algorithm. We then describe the use of this new retrieval to estimate the most representative snow model, using different types of snow morphologies, for the airborne observation conditions, performed by NASA's Cloud Absorption Radiometer (CAR).

Thirdly, we present a comprehensive comparison of the simulated reflectance (using retrieved snow grain size and shape as well as independent atmospheric data) with that from airborne CAR measurements in the visible (0.670 μm) and NIR (0.870 and 1.6 μm) wavelength range. The results of this comparison are used to assess the quality and accuracy of the radiative transfer model in the simulation of the reflectance in a coupled snow-atmosphere system.

Assuming that the snow layer consists of ice crystals with “aggregates of 8 column” ice habit, having an effective radius $\sim 99 \mu\text{m}$, we find that for a surface covered by old snow, the Pearson correlation coefficient, R , between measurements and simulations is 0.98 ($R^2 \sim 0.96$). For freshly fallen snow, assuming that snow layer consists of the “aggregate of 5 plate” ice habit with effective radius $\sim 83 \mu\text{m}$ and having surface inhomogeneity, the correlation is ~ 0.97 ($R^2 \sim 0.94$) in the infrared and 0.88 ($R^2 \sim 0.77$) in the visible wavelengths. Largest differences between simulated and measured values are observed in the glint area (i.e. in the angular regions of specular and near-specular reflection), with relative azimuth angles $\leq \pm 40^\circ$ in forward scattering direction. The absolute difference between the modeled results and measurements in off-glint regions with viewing zenith angle less than 50° is generally small $\sim \pm 0.025$ and does not exceed ± 0.05 . These results will help to improve the calculation of snow surface reflectance and relevant assumptions in the snow-atmosphere system algorithms (e.g. aerosol optical thickness retrieval algorithms in the Polar Regions).

30 **1 Introduction**

The extent and type of snow and ice cover have a significant impact on climate, as noted by Arrhenius over 100 years ago (Arrhenius, 1896). There is a positive feedback between decreasing surface temperature, an increase of snow and ice cover and an associated increase in planetary albedo, which then further decreases surface temperature and vice versa. Consequently, changes in snow and ice extent and morphology play a key role in climate change. Having accurate knowledge about snow/ice covered surface, is a prerequisite for identifying and quantifying changes in the climate (Schneider and Dickinson, 1974; Curry et al., 1995; Cohen et al., 2014; Kim et al., 2017; Wendisch et al., 2017; 2019).

In addition, during the past recent decades the Arctic region has warmed more rapidly than other regions. This phenomenon is known as the Arctic Amplification (AA) (Serreze and Barry, 2011). The analysis of the growing number of long-term records of the data products (e.g. the amount of trace gases, aerosol and cloud parameters), retrieved from passive and active satellite observations, provides potentially invaluable information to identify and quantify the evolution and consequences of AA (Wendisch et al., 2017).

Because of the magnitude of the scattering from snow, the use of remote sensing measurements above snow covered surfaces in the cryosphere, requires accurate models of the scattering and reflectance from snow surfaces. However, the current differences between simulated and measured reflectance in a coupled snow-atmosphere system, lead to systematic errors in the determination of the atmospheric constituents in particular

clouds and aerosol parameters but also trace gases (e.g. Istomina et al., 2010; 2012; Jafariserajehlou et al., 2019).

50 A large number of experimental and theoretical studies have been conducted measuring and modeling snow optical properties such as the angular distribution of reflected light over and within the snow surface and the subsequent derivation of snow albedo. The early measurements by Middleton and Mungal (1952) and the model of Dunkle and Bevans (1956) used to analyze the transmittance and reflectance of snow cover were the beginning of considerable efforts on this topic. Barkstrom (1972) formulated and solved the scattering problem for snow surfaces in terms of radiative transfer theory. Later, the comparison of reflectance from snow-covered
55 surfaces simulated by Radiative Transfer Models (RTM) with that of observation made substantial progress in our understanding of the angular distribution of reflectance above snow surface. (e.g. Wiscombe and Warren 1980; Warren et al., 1998; Arnold et al., 2002; Painter and Dozier, 2003; Kokhanovsky and Zege, 2004; Li and Zhou, 2004; Hudson et al., 2006; Hudson and Warren, 2007; Lyapustin et al., 2010; Kokhanovsky and Breon, 2012).

60 The reflection/scattering patterns of snow-covered surface can be summarized as follows: i) snow is not a Lambertian reflector in the visible and near infrared spectral region; its reflectance has anisotropic nature and the anisotropy increases with wavelength; ii) unlike other surface types (e.g. vegetation or soil) with a strong peak in back-scattering direction (the hot spot effect), snow has a strong forward peak for large viewing zenith angles (e.g. Gatebe and King, 2016); iii) The snow reflectance variation is larger in the principal plane (i.e. the
65 plane containing the Sun, surface normal and observation direction), than in the cross plane (i.e. the one perpendicular to principal plane) (Warren, 1982; Lyapustin et al., 2010; Kokhanovsky and Breon, 2012). However, the remaining discrepancies between simulated reflectance in a snow-atmosphere system and field measurements led to further investigations in the field of single scattering properties of snow grains (Mishchenko et al., 1999; Jin et al., 2008, Yang et al., 1998; 2003; 2013), surface roughness (Warren et al.,
70 1998; Hudson et al., 2006; Hudson and Warren, 2007; Lyapustin et al., 2010; Zhuravleva and Kokhanovsky, 2011) and atmospheric correction methods (Lyapustin et al., 2010). Despite substantial improvements, the uncertainties in our understanding of the microphysical and macroscopic properties of snow are an unresolved issue for RTMs, ray-tracing and climate models. For example, the current state of the art RTMs yield much more anisotropic reflectance behavior for snow in the glint region than observed in reality (Zhuravleva and
75 Kokhanovsky, 2011; Lyapustin et al., 2010; Hudson and Warren, 2007; Warren et al., 1998). These studies either focus on the snow reflectance at the surface, employing an atmospheric correction method (Leroux et al., 1998; Kokhanovsky and Zege, 2004; Kokhanovsky et al., 2005; Lyapustin et al., 2010; Negi and Kokhanovsky,

2011) or consider the atmospheric effects without in-depth investigations of the surface parameters (Aoki et al., 1999; Hudson et al., 2006; Kokhanovsky and Breon, 2012). A comprehensive study and investigation of both
80 snow layer and atmosphere parameters in a coupled snow-atmosphere system has not yet been undertaken but is required to improve the accuracy of remote sensing retrieval algorithms for aerosol and cloud in the Arctic region (Istomina et al., 2010; 2012; Jafariserajehlou et al., 2019).

The intent of this paper is to: i) study the sensitivity of scattering and reflectance in the coupled snow-atmosphere system to both surface and atmospheric parameters; ii) retrieve the most representative ice crystal
85 morphology by applying a snow grain size and shape retrieval algorithm to measured reflectance; iii) evaluate the ability of a phenomenological RTM, to reproduce the measured reflectance over the spectral range $0.34 \mu\text{m} - 1.649 \mu\text{m}$ at all available observation directions using the retrieved atmospheric and snow parameters.

In this study, we use the RTM SCIATRAN (Rozanov et al., 2014) which is a well validated phenomenological RTM, and the airborne observations of reflectance, acquired by Cloud Absorption
90 Radiometer (CAR). The CAR measurements were made during the Arctic Research of the Composition of the Troposphere from Aircraft and Satellite (ARCTAS) spring 2008 campaign over Barrow/Utqiagvik, Alaska. Further information about the atmospheric parameters during the ARCTAS campaign was taken from available AERONET and satellite data.

The paper is organized as follows: in the next section, we present the theoretical background and terminology
95 used to calculate the angular distribution of reflectance in a snow-atmosphere system. In sect. 3 and 4, we introduce and explain the measurements and the simulation methods. In sect. 5, the sensitivity of reflectance to the underlying snow layer and atmospheric parameters is investigated. In sect. 6, the results of applying the two-stage snow grain size and shape retrieval algorithm are presented. In sect. 7, the results of the reflectance simulations are compared to CAR measurements. Finally, conclusions are drawn in sect. 8. Appendix contains
100 detailed description of the snow grain size and shape retrieval algorithm used in the study.

2 Theoretical background

To describe the directional signature of reflectance over different surface types, the Bidirectional Reflectance Distribution Function (BRDF) as defined by Nicodemus (1965), is the commonly used reflectance quantity. The term BRDF describes the reflection of incident solar radiation from one direction to another direction
105 (Nicodemus 1965). The mathematical form of BRDF is expressed as (Nicodemus et al., 1977; Schaepman-Strub et al., 2006):

$$BRDF_{\lambda} = \frac{dL_r(\theta_i, \varphi_i, \theta_r, \varphi_r; \lambda)}{dE_i(\theta_i, \varphi_i; \lambda)} [sr^{-1}], \quad (1)$$

where L_r is the reflected radiance, θ and φ are the zenith and azimuth angles, respectively. The subscript i corresponds to the incident and r to the reflected beams. E is the incident surface flux (irradiance) and λ is the wavelength. However, the BRDF is not a directly measurable quantity because of its being formulated as a ratio of infinitesimal quantities (Nicodemus et al., 1977; Schaepman-Strub et al., 2006). Nicodemus et al. (1977) provided an extensive description of reflectance terminologies and measurable quantities e.g. the Bidirectional Reflectance Factor (BRF), the Hemispherical Directional Reflectance Factor (HDRF), the Directional Hemispherical reflectance (DHR), etc. According to Nicodemus et al. (1977) and Schaepman-Strub et al. (2006) each of the terms is defined for the specific illumination and reflectance geometries for which, the reflectance properties are measured (e.g. satellite, airborne or laboratory measurement conditions). Following the method of Gatebe and King (2016), the effective BRDF at a horizontal (flat) reference plane is defined as:

$$BRDF_{\lambda}^e = \frac{\Delta L_r(\theta_i, \varphi_i, \theta_r, \varphi_r; \lambda)}{\Delta E_i(\theta_i, \varphi_i; \lambda)} = \frac{\Delta L_r(\theta_i, \varphi_i, \theta_r, \varphi_r; \lambda)}{\Delta L_i(\theta_i, \varphi_i; \lambda) \cos \theta_i \Delta \omega_i} [sr^{-1}], \quad (2)$$

where $BRDF_{\lambda}^e$ is as an average of the BRDF over an appropriate area, angle and solid angle for specific observation geometry; $\Delta \omega_i$ is a finite solid angle element. The validity of this approximation relies on the experimental evidence that the BRDF is not significantly influenced by the following effects: the finite intervals of area, angle, solid angle and the distribution function; sub-surface scattering; radiation parameters such as wavelength and polarization, fluorescence etc. (i.e. significant variations do not occur within small intervals, see Nicodemus et al., 1977; Gatebe and King, 2016). As a result, the $BRDF_{\lambda}^e$ is determined by:

$$BRDF_{\lambda}^e = \frac{L_r^e(\theta_i, \theta_r, \Delta \varphi)}{F_{0,\lambda} \cos \theta_i}, \quad (3)$$

where L_r^e is the measured radiance, $F_{0,\lambda}$ is the solar irradiance incident at the top of atmosphere (TOA). Often, it is helpful to have a description of the difference between the measured surface reflectance and a Lambertian reflector; in such a case the equivalent Bidirectional Reflectance Factor BRF_{λ}^e , which is $BRDF_{\lambda}^e$ multiplied by π is more representative.

130 To isolate the reflectance properties of the surface and derive BRF_{λ}^e or $BRDF_{\lambda}^e$ just above the surface, we need to apply atmospheric correction methods on the measured radiance at TOA or flight altitude (e.g. by using knowledge of the atmospheric scattering or absorption applying RTMs). This removes the four atmospheric contributions from the measured radiance at TOA or flight altitude (Schaepman-Strub et al., 2006): the contribution of light scattered by the atmosphere, i) before the solar radiation has reached the surface, ii) after
 135 being reflected by the surface, iii) before and after reaching the surface and iv) the atmospheric path radiance.

However, most of the atmospheric contributions in measurements close to the surface are negligible (except diffuse component-number ii) and measured quantities represent the “at surface” radiance (Schaepman-Strub et al., 2006). Sensitivity studies have demonstrated that atmospheric contributions to the CAR channel observations range from 3 to 12% depending on wavelength in the range of 0.381 to 2.324 μm (Soulen et al.,
 140 2000). Consequently, previous studies presented either the BRFs in a surface-atmosphere system at flight altitude without atmospheric correction (Soulen et al., 2000) or the BRFs right above the surface after atmospheric correction (Gatebe et al., 2005; Gatebe and King 2016).

The atmospheric correction methods relies on different assumptions by which several source of uncertainties should be taken into account. In this study, to avoid such uncertainties, we do not apply an atmospheric
 145 correction to the measurements (radiance $L_{r,h}$) at flight altitude (h). Instead, we calculate and use the reflectance at flight altitude by the following equation:

$$R = \frac{\pi L_{r,h}(\theta_i, \theta_r, \Delta\phi)}{F_{0,\lambda} \cos\theta_i} \quad (4)$$

where $L_{r,h}$ is the measured radiance at flight altitude. All reflectance/ BRF_{λ}^e values at flight altitude in this study represent R in Eq. 4 and are referred to as “reflectance factor” in the snow-atmosphere system.

150 In the simulation of the reflectance factor in a coupled snow-atmosphere system, we need to account for atmospheric effects contribution properly. For this reason, we take independent data about atmospheric parameters (Aerosol Optical Thickness (AOT) and gases absorption) from ground-based and space-borne measurements. We select the data with the closest spatial and temporal interval actual airborne measurements. We discuss more details of the atmospheric data and their application to the simulation routine in sect. 3 and 4.
 155 To estimate BRF_{λ}^e just above the surface, further atmospheric correction is needed. We assume the reflectance factor at flight altitude is a good estimation of BRF_{λ}^e just above the surface at infrared wavelengths where atmospheric scattering is negligible.

3 Measurements

CAR is an airborne instrument, developed at NASA's Goddard Space Flight Center. It has been used during several field campaigns around the world since 1984 up to present. CAR has been used to measure the single scattering albedo of clouds, the bidirectional reflectance of various surface types and acquiring imagery of clouds and the Earth's surface. For this study, we used CAR data from the ARCTAS campaign conducted at Elson Lagoon, near Barrow/Utqiagvik, Alaska, in April 2008 as part of the International Polar Year (Lyapustin et al., 2010; Gatebe and King, 2016). The goal of ARCTAS was to study physical and chemical processes in the Arctic atmosphere and (e.g. long-range transport of pollution to the Arctic) and surface parameters (e.g. snow reflectance angular variation). The P-3B aircraft carried CAR instrument and was deployed by NASA from Fairbank. Fig. 1 shows the flight track on 7th of April 2008. The date, location, measurement geometry and available atmospheric parameters during the measurements used in this study are presented in Table 1.

The unique design of CAR provides simultaneously both up-welling and down-welling radiances at 14 spectral bands (Table 2) located in the atmospheric window regions of UV, visible and near-infrared from 0.34 μm to 2.3 μm comprising important wavelengths relevant for remote sensing applications such as aerosol retrievals. Through a rotating scan mirror, the instrument provides viewing geometries suitable for measurements needed for BRF calculation. CAR collects data by a mirror rotating 360° in a plane perpendicular to the direction of flight through a 190° aperture that allows acquiring data from local zenith to nadir or horizon to horizon with an angular resolution of 1°. The high angular/spatial resolution of 1° in both viewing zenith and azimuth angles allows the estimation of the anisotropy of the reflectance in the snow-atmosphere system with high accuracy.

The spatial resolution of CAR depends on the flight altitude e.g. 10 m² and 18 m² at nadir for 600 m and 1000 m flight altitude, respectively, which increases with the viewing zenith angle (VZA) e.g. 580 m² at 80° VZA for 1000 m flight altitude. The capability of acquiring data at different altitudes (~ 200, 600 and 1700 m) enables us to evaluate the sensitivity of reflectance with respect to atmospheric effects in RTM simulations.

Examples of calculated reflectance factor values using Eq. (4) from CAR measurements on 7th of April, 2008 at Elson Lagoon (71.3° N, 156.4° W) are shown in Fig. 2 and Fig. 3. As we can see in these two figures, in spite of the influence of the atmospheric scattering and absorption, the general features of the snow BRF are clearly observable in polar plots as well as principal and cross plane plots: i) the decrease of snow reflectance with increasing wavelength due to the increasing absorption by snow at longer wavelengths; ii) the increase of the snow BRF as a function of VZA and the strong forward scattering peak in the principal plane at large VZA; iii)

the smaller angular variation of the BRDF at cross plane compared to the principal plane, though the reflectance values increase with VZA. The snow surface spatial inhomogeneity decreases with increasing altitude due to the change of spatial resolution with altitude (Gatebe and King, 2016; Lyapustin et al., 2010). Accordingly, at poorer spatial resolution, spatial homogeneity are more efficiently averaged as can be seen in Fig. 2 at flight altitude of 1700 m compared to 206 m in which we have higher spatial resolution.

To account for aerosols, we use the Aerosol optical thickness (AOT) data acquired by the nearby Aerosol Robotic Network (AERONET) sun-photometer at Barrow/Utqiagvik during the CAR measurement time. AERONET is a globally distributed network and provides long-term and continuous ground-based measurements of the total column aerosol optical thickness derived from the attenuation of sun light and provided often at high temporal resolution of 15 minutes. AERONET AOT data are provided at 0.5 μm and 0.6 μm wavelengths. We use the Ångström exponent to calculate AOT values at the reference wavelength (0.55 μm) required for the SCIATRAN simulation. Table 1 shows the calculated AOT at 0.55 μm based on AERONET data for Barrow/Utqiagvik at the closest time to the CAR airborne measurements. Aerosol condition and its chemical and optical properties have been measured continuously at Barrow, Alaska, during different seasonal periods (Quinn et al., 2002). Previous studies indicate the largest contribution from sea salt, non-sea-salt sulfate and mineral dust. The average contribution of black carbon is very small compared to other aerosol types (Udisti et al., 2020). During the haze season (January to April), sea salt plays the dominant role in controlling light scattering in wintertime and non-sea salt sulfate in spring (Quinn et al., 2002). The increase on nss-sulfate in January to May is the long-range transport of anthropogenic primary nss sulfate besides the long-range transport of anthropogenic SO_2 and its photo-oxidization to nss-sulfate with increase of light levels, and the local production of biogenic nss-sulfate.

To account for ozone absorption, we use knowledge of the ozone total column amount retrieved from the space borne measurements by using the University of Bremen weighting function DOAS (WFDOAS) algorithm version 4 (Weber et al., 2018). This data set (covering from 1995-present) consists of merged total ozone column data retrieved by WFDOAS from Global Ozone Monitoring Experiment (GOME), Scanning Imaging Absorption Spectrometer for Atmospheric Chartography (SCIAMACHY), and GOME-2A. In this paper, the ozone total column data are selected using the criteria of having smallest temporal and spatial differences with CAR data. For nitrogen dioxide, we use vertical column information from the SCIATRAN database obtained from a 2D chemical transport model developed at University of Bremen (Sinnhuber et al., 2009).

The derived AOT and trace vertical column have been used in the simulation of radiative transfer processes in the snow-atmosphere system.

4 Simulations

220 SCIATRAN is a software package for radiative transfer modeling, developed at the Institute of Environmental
Physics (IUP), University of Bremen (Rozanov et al., 2002; 2014) and freely available at [http://www.iup.uni-
bremen.de/sciatran/](http://www.iup.uni-bremen.de/sciatran/). The SCIATRAN package has been used in a variety of remote sensing studies to simulate
radiative transfer processes in the wide spectral range from the ultraviolet to the thermal infrared (0.18 μm - 40
 μm), assuming either a plane parallel or a spherical atmosphere (Rozanov et al., 2014).

225 In this paper, to calculate reflectance factor values, SCIATRAN assumes that the snow is a layer with an
optical thickness of 1000 and a geometrical thickness of 1 m composed of ice crystals of different morphologies
and placed above a black surface. This assumption was successfully validated by Rozanov et al. (2014). The
snow layer is assumed to be vertically and horizontally homogeneous and composed of a monodisperse
population of ice crystals. The impact of impurities in the snow (e.g. black carbon) is neglected in this study. To
230 simulate the radiative transfer through a snow layer, the single scattering properties of ice crystals including
extinction and scattering efficiencies, single scattering albedo and phase functions need to be defined in
SCIATRAN. All these parameters are dependent on the wavelength, size and shape of the particle (Leroux et al.,
1999). Recently, a new data library of basic single scattering properties of nine ice crystal shapes/habits
developed by Yang et al. (2013) has been incorporated in the SCIATRAN model (Pohl et al., 2020). This
235 database comprises a full set of single scattering properties at wavelengths from the UV to the far IR for the
following nine ice crystal morphologies: droxtal, column and hollow column, aggregate of eight columns,
plates, small aggregate of five plates, large aggregate of ten plates, hollow and solid bullet rosettes. More
detailed information about the ice crystal shapes and sizes can be found in Yang et al. (2013). In addition to the
above-mentioned nine ice crystals, optical parameters for triadic Koch fractal (referred to as fractal in this paper)
240 particles are used as well (Macke et al., 1996; Rozanov et al., 2014). The fractal particle model uses regular
tetrahedrons as its basic elements. In this study, we use the second generation fractals as described in Macke et
al. (1996) and Rozanov et al. (2014).

In SCIATRAN, the snow grains are specified by their single-scattering properties of sparsely distributed
particles. Namely, the snow grains are assumed to be in the far field zones of each other and will thus scatter the
245 light independently. For a snow layer, the snow grains can be located in each other's near-field, resulting in
interactions between the scattered electromagnetic fields of neighboring particles which leads to modification of
single-scattering properties (Mishchenko, 2014; Mishchenko, 1994). The impact of near-field effect was
investigated in Pohl et al. (2019) using the modified single scattering properties of sparsely distributed particles

as suggested in Mishchenko (1994). The comparison of snow BRFs calculated assuming sparsely or densely
250 packed snow layers shows that the maximum difference does not exceed 0.015% (Pohl et al., 2019). Therefore,
this effect was ignored in radiative transfer calculations through the snow layer.

To account for atmospheric effects, SCIATRAN incorporates a comprehensive database containing monthly
and zonal vertical distribution of trace gases e.g. O₃, NO₂, SO₂, H₂O, etc., spectral characteristics of gaseous
absorbers, vertical profiles of pressure and temperature and molecular scattering characteristics (see Rozanov et
255 al., (2014) for details). To account for scattering and absorption by aerosols over snow in SCIATRAN, the
optical characteristics of aerosol particles and vertical distribution of aerosol number density are required. In this
study we use Moderate Resolution Imaging Spectrometer (MODIS) collection 5 aerosol parameterization (Levy
et al., 2007) as an internal database in SCIATRAN. Levy et al. (2007) developed a framework for connecting
the aerosol micro-physical properties such as the refractive index and size distribution to the AOT at 0.55 μm.
260 Using AOT from ground-based measurements of AERONET at Barrow/Utqiagvik as mentioned and selecting
one of the aerosol types, the Mie code incorporated into SCIATRAN is employed to calculate aerosol extinction
and scattering coefficients. In this study, the vertical profile of aerosol number density as an “exponential
vertical distribution” for a height of 3.0 km is used.

For the conditions described above, the radiative transfer calculations are performed at a source-target-sensor
265 geometry extracted from the airborne measurements at solar zenith angle of 70.23°, 69.11°, 67.68° and 62.11°;
viewing zenith angle 0° - 70° and relative azimuth angle 0° - 360° with an angular resolution of 5° and at four
different altitudes of 181 m, 206 m, 647 m and 1700 m. More detailed information about atmospheric and snow
layer parameters are given and discussed separately in the following section.

5 Sensitivity of reflectance to the snow morphology and atmospheric parameters

270 The measured reflectance in the visible and NIR spectral range over a snow field depends on the relative
importance of the absorption and scattering radiative transfer processes in the atmosphere and snow layer. In
this section, we investigate the sensitivity of the reflectance on the radiative transfer through the atmosphere and
the snow at the selected wavelength bands: i) 1.649 μm because of the high sensitivity of this wavelength to
snow grain properties; and ii) 0.677 and 0.873 μm wavelengths because of the relatively high and differing
275 sensitivities at these wavelengths to the atmospheric conditions and being used for aerosol optical thickness
retrievals.

5.1 Impact of snow: size and shape of ice crystals

To study the influence of ice crystal morphology on the radiation field above snow-covered surfaces, we perform the simulation at 1.649 μm for three important reasons (Leroux et al., 1998):

- 280 i) the absorption of ice crystals is small or negligible at the selected wavelengths in the visible domain of the spectrum. In contrast, in the near-infrared range, due to the large absorption of ice crystals at these wavelengths, the snow reflectance is significantly affected by the snow grain size; the larger the particle, the smaller the reflectance because of larger absorption and stronger forward scattering;
- ii) the BRF properties of snow at 1.649 μm are closer to that for single scattering behavior and it is linked to the
285 phase function, which strongly depends on the shape of ice crystals;
- iii) the impact of the atmosphere (absorption by CO_2 and H_2O and diffuse incident irradiance) at 1.649 μm is negligible.

To illustrate the high sensitivity of radiation field to the varying size of ice crystals at 1.649 μm , we simulated snow reflectance factor at principal and cross planes assuming nine ice crystal morphologies with varying sizes
290 (here size refers to maximum dimension/edge length) 60 ~ 10000 μm and three different roughness (smooth surface: 0, moderate surface roughness: 0.03, severe surface roughness 0.5), for further information see Yang et al. (2013). Fig. 4 shows the simulated reflectance factor versus the VZA in the principal plane (as the most sensitive and representative direction for the largest changes of reflectance) using severely roughened morphology. As can be seen in Fig. 4, the reflectance factor strongly changes with the size of ice crystals from
295 60 to 10000 μm . The equivalent effective radius¹ is shown besides the maximum lengths of ice crystals in Fig. 4. Differentiating between various shapes has the largest effect in forward scattering ($\varphi=0^\circ$) and lesser effect in backward scattering direction ($\varphi=180^\circ$). The results indicate that the effect of changing size is larger than the impact of differentiating between various shapes of ice crystals at this wavelength.

Using the “aggregate of 8 columns” shape and changing maximum dimension from 60 μm to 10000 μm result
300 in reflectance decrease of ~ 40 % at nadir (VZA ~ 0°) and more than 80 % in forward scattering direction (at VZA of 60°) which is considerably large. If we change only the shape of snow grain from “aggregate of 8 columns” to the “droxtal”, but we keep the size (largest dimension) as it is (e.g. 300 μm) this change provides a noticeable decrease of ~ 30% in reflectance at forward scattering direction for a viewing zenith angle of 60° and leads to a much weaker forward peak. Noteworthy is, that the plate shape cannot reproduce the enhancement in

¹ Effective radius = $3/4 \times (V_{\text{tot}}/A_{\text{tot}})$; V_{tot} : total volume and A_{tot} : the total projected area of ice per unit volume of air (Baum et al., 2014).

305 backward direction (typical for a BRF over snow) as strong as the “aggregate of 8 columns” or the “droxtal”
shape cause. Using the “aggregate of 5 and 10 plates” leads to larger reflectance in all directions compared to
the single “plate” shape. However, the analysis of simulation results at cross plane (not shown here) indicates
that, the impact on the reflectance pattern, originating from the specific shapes of the ice crystals is relatively
small compared to the impacts at principal plane.

310 The large range of changes of the reflectance in both the principal and cross planes, when using different ice
crystal morphologies highlights the importance of having accurate a priori knowledge or estimation of size and
shapes of the ice crystals to accurately reproduce measurements. In our study, due to the lack of such
information from in situ measurements, we estimate the size of ice crystals for each selected crystal shape
separately to have a priori knowledge of ice crystal properties and limit the differences between the simulated
315 and measured reflectance. The detailed explanation and results are given in sect. 6.

5.2 Impact of atmosphere: scattering and absorption by aerosol and gases

The incident radiation is composed of direct sunlight and the diffuse radiation from the sky (Aoki et al., 1999).
To take the atmospheric absorption and scattering into account, we assume an atmosphere over the snow layer,
which contains: i) Rayleigh scattering (scattering by air molecules), ii) gaseous absorption and iii) absorption
320 and scattering by aerosols. Therefore, in this section, absorption bands e.g. 0.677 μm are selected to evaluate the
impact of the atmosphere. We calculate the reflectance factor at 0.677 μm under three different conditions,
assuming a model atmosphere governed: i) by Rayleigh scattering; ii) identical to i) but with absorption by
ozone (O_3) and nitrogen dioxide (NO_2); iii) identical to ii) but including aerosol. The calculations are performed
assuming the following properties of the atmosphere and snow layer:

325 i) Vertical profile of nitrogen dioxide, pressure and temperature are selected according to a 2D chemical
transport model (Sinnhuber et al., 2009) incorporated in SCIATRAN;
ii) Total vertical column of ozone as well as AOT are set according to Table 1;
iii) Snow layer is composed of ice crystals having the shape “aggregate of 8 column”, maximum dimension of
650 μm and severely roughened crystal surface.

330 Fig. 5 shows the impact of the atmosphere and the difference between measured and simulated reflectance
factor values at three different altitudes: 206, 647 and 1700 m; for the 3 scenarios. The reflectance reduction at
647 m flight altitude due to gaseous absorption is the smallest $\sim 5\%$ close to the nadir region and becomes larger
 $\sim 10\%$ in forward scattering direction which decreases to $\sim 8\%$ at 1700 m altitude. At this wavelength, ozone

with vertical optical depth (VOD) of 1.6×10^{-2} has a much larger contribution to gaseous absorption as compared
335 to that of NO_2 with VOD of 3.95×10^{-5} .

The reflectance for an atmosphere containing three types of aerosol (weakly/moderately/strongly absorbing
aerosol) and without aerosol (containing only Rayleigh and gaseous absorption) are presented in Fig. 5. For
more information on aerosol typing used in this study see Levy et al. (2007). The changes in reflectance due to
weakly absorbing aerosol with an AOT of 0.11 (measured by AERONET) at 206 m flight altitude are $\sim 5\%$ at
340 nadir and increase in forward scattering direction to $\sim 13\%$. The strongly absorbing aerosol (at the same AOT of
0.11) reduces the reflectance by $\sim 7\%$ at nadir and $\sim 20\%$ in forward scattering direction. At 1700 m, the
reflectance decreases by 6% at nadir and 7% in forward scattering direction. The differences between the three
aerosol types does not lead to changes in reflectance, which are larger than 5% in or close to nadir areas. In
summary, an atmosphere containing Rayleigh scattering, absorption by ozone (O_3) and nitrogen dioxide (NO_2)
345 and weakly absorbing aerosol is the best representation of the atmospheric conditions for our case study.

6 Retrieval of snow grain size and shape

In the previous section, we showed that having adequate a priori information about snow surface and
atmosphere is necessary to calculate reflectance factor of sufficient accuracy. In contrast to the atmospheric
parameters available from independent sensors and models, a priori knowledge about ice crystal size and shape
350 for the underlying snow layer is not typically available. To estimate the optimal ice crystal morphology we used
a snow grain size and shape retrieval algorithm, by minimizing the difference between the measured and
simulated reflectance factor (See appendix A for details). Here size refers to effective radius of the ice crystal.
The retrieval algorithm is applied to measurements at principal and cross planes at $1.649 \mu\text{m}$ assuming different
shape and crystal surface roughnesses. To find the best representative shape and size, the bias and Root Mean
355 Square Error (RMSE) between the measured and simulated reflectance factor were determined for each case
study.

Fig. 6 shows one example of the comparison between measured and simulated reflectance factor at principal
and cross planes. The absolute uncertainty of CAR measurements is within 5% and shown by uncertainty
envelope. The accuracy of our radiative transfer calculations is estimated to be in the range of 0.1%. Based on
360 comparison, one can state that the angular reflectance pattern of the CAR measurement on the 7th of April 2008
at Elson Lagoon is reproduced by SCIATRAN successfully. The highest accuracy is obtained by assuming ice
crystals as “an aggregate of 8 columns” with severely roughened crystal surface at an effective radius of $98.8 \mu\text{m}$
(corresponding to maximum dimension of $650 \mu\text{m}$). In this case, the largest and smallest discrepancies

appear in the forward scattering direction and close to nadir ($VZA < \pm 25^\circ$), respectively. The overall RMSE and
365 bias between measurements and simulation at principal plane is 6.9 % and 2.7 % respectively. A lesser degree of
agreement between simulated results and measurements are provided by using “column” and fractal shapes with
an RMSE of 7.3% and 9.75%, respectively. The largest difference between measurements and simulations is
observed for the case using “droxtal” shape with an RMSE $\sim 25.54\%$.

We also retrieved effective radius of ice crystal using CAR data for fresh fallen snow on the 15th of April
370 2008. Due to the existing surface horizontal inhomogeneity for the case of fresh snow acquired at lower flight
altitude ~ 181 m, larger differences between simulated and measured reflectance are expected, as compared to
the old snow case on the 7th of April 2008. The results are shown in Fig. 7. Unlike the old snow case presented
in Fig. 6, the “aggregate of 8 columns” shape does not optimally represent the ice crystals of this particular day.
Rather, a reflectance simulated by using an “aggregate of 5 plates” as the ice crystal shape provides the
375 minimum RMSE $\sim 12.85\%$ between measurement and simulation results. “Aggregate of 10 plates” and fractal
provide the second and third most representative shapes with an RMSE of $\sim 13.16\%$ and 14.69% respectively.
The results obtained by using the “droxtal” ice crystal shape exhibit large differences in both of forward and
backward scattering directions with RMSE of 34.1 %.

Though the real nature of ice crystal shape at the time of measurement is not known to us, the impact of
380 temperature and supersaturation on morphology of snow grain particles has been debated in previous studies
(Slater and Michaelides, 2019; Shultz, 2018; Libbrecht, 2007; Bailey and Hallett, 2004; Yang et al., 2003).
Based on the relationship between temperature and snow grain morphology, the column-based shapes are the
dominant ice crystal morphology in environments with temperatures higher than -10°C whereas plates are
dominant if the temperature is less than -10°C . Though, more investigation is needed especially to account for
385 the temperature profile at the exact time of snowfall, our findings with respect to the most representative shape
for each case study agree with this argument. The temperature range during CAR measurements at 6-7th of April
2008 is from -20 to -5°C . Based on our results the “aggregate of 8 columns” is the most representative shape for
measurements conducted on this day. On 15th of April 2008 when the temperature range changes to -23 to -17°C ,
mainly plate-based ice crystal shapes are expected for such low temperatures and our results confirm this
390 argument. In addition, the existence of droxtal ice crystals during the measurement is less probable because very
low temperatures ($\sim -50^\circ\text{C}$) are needed to form droxtal or quasi-spherical ice crystals (Yang et al., 2003). The
temperature dependence of the ice crystal morphologies explains in part why droxtal shaped ice crystals do not
capture the derived snow reflectance values from CAR measurements in any of our scenarios. With respect to
size of ice crystals, we do not compare fresh and old snow cases because it is important to note that the date of

395 old snow case is before fresh snow. This means the studied old snow case is not the aged fresh snow case. Therefore, the change of ice crystal size with its age is not studied in the scope of this paper.

A summary of retrieved effective radii using different ice crystal shapes and corresponding bias and RMSE values is presented in Table 3. The ice crystals with minimum RMSE value at 1.649 μm are underlined and selected to be used for subsequent calculations of reflectance factor at 0.677, 0.873 μm . In Fig. 8, the
400 importance of ice crystal shape selection for the snow grain size retrieval and the snow reflectance calculation is highlighted. The measurements were selected from the old snow and fresh snow cases. The effective radius is retrieved only at 1.649 μm and then has been used to calculate the reflectance factor at 0.677 μm and 0.873 μm . The results are presented in Fig. 8 with corresponding RMSE and bias values in the principal plane. The uncertainty of effective radius retrieval is estimated to be $\sim 10\%$ on the base of optimal estimation technique and
405 is shown by gray envelope in Fig. 8. It can be seen that the retrieved effective radius value changes from shape to shape. The difference in retrieved effective radius generally does not exceeds 40 % but in the case of the plate ice crystals the retrieved effective radius is $\sim 70\%$ smaller than the other shapes e.g. aggregate of 8 columns. This is a significantly large difference. However, these results are presented for the principal plane where the maximum differences between simulation and measurement is expected. Therefore, the overall bias and RMSE
410 value on all azimuth direction is smaller than presented here. It can be seen that the RMSE values at 0.677 μm and 0.873 μm are significantly smaller than that at 1.649 μm . This is explained by the high reflectance values at these wavelengths and therefore the larger denominator in RMSE formula, in which the difference of measured and simulated reflectance factor is divided by measured reflectance.

7 Comparison of measured and simulated reflectance factor

415 In this section we present results of the comparison of measured and simulated reflectance factor in the snow-atmosphere system. The simulations, which used the results and findings described in the previous section were performed: assuming an atmosphere containing O_3 , NO_2 , weakly absorbing aerosol as described in Table 1. The snow layer is assumed to be comprised of “aggregate of 8 column” ice crystals with a maximum dimension of 650 μm (effective radius 99 μm) for the case of old snow, and “aggregate of 5 plates” ice crystals with a
420 maximum dimension of 725 μm (effective radius 83 μm) for the case of fresh snow.

In Fig. 9, the difference between the simulated and measured reflectance factor at 0.677 and 1.649 μm is small on average, being less than 0.025 in regions of small VZA and not exceeding ± 0.05 for larger VZA $< 50^\circ$. These values are larger at 0.873 μm ; the maximum difference reaches $\sim \pm 0.05$ for small VZA. The difference between SCIATRAN simulation values and those of the measurements is pronounced in the forward scattering

425 region where $|\Delta\phi| < 40^\circ$. Fig. 10 is the same plot as Fig. 9 but for fresh snow. The differences between
SCIATRAN simulations and CAR measurements of the reflectance factor are less pronounced in the glint
region, as compared to those for the old snow.

To assess the accuracy of simulations over all azimuth angles, the correlation plot and the Pearson correlation
coefficient between measured and modelled reflectance factor are shown in Fig. 11. As it is shown in Fig. 11,
430 the correlation coefficient between reflectance measurements over old snow and simulation is high, ~ 0.98 . We
consider that surface inhomogeneities and related larger shadowing effects at measurement altitude of 181 m,
explain why the correlation decreased to 0.88 at $0.677 \mu\text{m}$ (for the case of old snow, acquired at 647 m flight
altitude, surface inhomogeneities are smoothed and therefore the old snow case is less affected by surface
inhomogeneities). However, in Fig. 11, at $1.649 \mu\text{m}$ correlation coefficient is high ~ 0.97 for the case of fresh
435 snow, possibly because of their being less sensitivity of this channel to shadowing and atmospheric scattering
effects.

8 Conclusion

In this study, our objective was to assess the accuracy of the simulation of the reflectance in a snow-atmosphere
system taking different snow morphology and atmospheric absorption and scattering into account. For this we
440 used a state of the art RTM, SCIATRAN, which used explicit models of the snow layer and the airborne CAR
measurements.

The airborne CAR data were acquired by NASA over Elson Lagoon at Barrow/Utqiagvik, Alaska, during the
ARCTAS campaign in spring 2008. The spectral coverage of the airborne measurements is wide ($0.3\text{-}2.30 \mu\text{m}$)
comprising important wavelengths relevant for remote sensing applications such as aerosol retrievals which
445 could benefit from the results of this study. Measurements obtained at different flight altitudes ($\sim 200, 600$ and
 1700 m) provide an opportunity to investigate the sensitivity of simulated reflectance to atmospheric parameters.

The SCIATRAN RTM (a phenomenological RTM) was used to simulate the reflectance factor in the snow-
atmosphere system and its changes for different snow morphologies (i.e. snow grain size and shape). These
simulations take atmospheric scattering and absorption explicitly into account. We investigated the sensitivity of
450 reflectance in the snow-atmosphere system to snow grain size and shape. We have shown that the selection of
the most representative shape and size of the nine ice crystals used in SCIATRAN to describe the snow surface
is essential to minimize the difference between simulations and measurements.

To obtain a priori knowledge of snow morphology, we use the snow grain size and shape retrieval algorithm
and apply it to CAR data. In our case study at Barrow/Utqiagvik, the simulated reflectance factor assuming ice

455 crystals with aggregate composed of 8 columns shape agreed well with measurements for the old snow case,
having RMSE of 6.9 % and average bias of 2.7 % with respect to the measured CAR reflectance in the principal
plane where the largest discrepancies are expected. For the case of freshly fallen snow, an aggregate of 5 plates
shape was the most representative ice crystal having RMSE values of 12.8 % and a bias of 11.23 % with respect
to the measured CAR reflectance. The data for the freshly fallen snow case were acquired at 181 m. Larger
460 differences as compared to the older snow case at 647 m are attributed to surface inhomogeneity. The surface
inhomogeneity most likely originate from sastrugi. Simulation, in which the snow layer was comprised of ice
crystals with a droxtal shape (being semi-spherical particles) did not yield accurate reflectance for the snow-
atmosphere system in any of our case studies. We showed that using the knowledge from studies of the
temperature dependence of ice crystal morphologies agrees with our findings with respect to the most
465 representative ice crystal size and shape for our case studies.

In our study, the simulated patterns of the reflectance factor with respect to spectral and directional signatures
produce well the measurements, as evidenced by the high correlation coefficients in the range of 0.88 ~ 0.98
between measurements (old and fresh snow) and simulation at the selected wavelengths of 0.677, 0.873 and
1.649 μm . In the off-glint regions $|\Delta\phi| > 40^\circ$ and $VZA < 50^\circ$, the overall absolute difference between the
470 modeled reflectance factor from SCIATRAN and CAR measurements is below 0.05. This absolute difference in
off-glint area is smaller in the short wave infrared as compared to visible. It should be noted here that the
reflectance of the snow is lower in the short wave infrared compared to the visible.

In summary, the approach shows the high accuracy of the phenomenological SCIATRAN RTM in simulating
the radiation field in the snow-atmosphere scenes for off-glint observations. The results are applicable for the
475 inversion of snow and atmospheric data products from the satellite or airborne passive remote sensing
measurements above snow. To mitigate the relatively larger differences between measurements and simulation
for glint condition as compared to off-glint region, the use of a vertically inhomogeneous snow layer consisting
of different ice crystal shapes and sizes is proposed.

This research has been undertaken as part of the investigations in the framework of trans-regional (AC)³
480 project (Wendisch et al., 2017) that aims to identify and quantify different parameters involved in rapidly
changing climate in the Arctic. In this respect, the analysis of this study will be used to improve the assumptions
made for reflectance in snow-atmosphere system in the algorithms designed to retrieve atmospheric parameters
(such as AOT) above Polar Regions.

Appendix

485 For the selected snow models using different ice crystal morphologies, the variation of the snow reflectance $R(\lambda, \Omega)$ at wavelength λ and direction Ω with respect to the variation $\delta r_e(z)$ of the effective radius profile $r_e(z)$ along the vertical coordinate z within snow layer can be presented, neglecting nonlinear terms, by the following equation:

$$R(\lambda, \Omega) = R_0(\lambda, \Omega) + \int_0^{Z_t} W_r(z, \lambda, \Omega) \delta r_e(z) dz, \quad (1)$$

490 where $R_0(\lambda, \Omega)$ and $R(\lambda, \Omega)$ are the reflection functions calculated assuming an effective radius profile $r_e(z)$ and $r_e(z) + \delta r_e(z)$ respectively. The angular variable $\Omega = \{\theta_0, \theta, \varphi\}$ comprises a set of variables: θ_0 is the solar zenith angle, θ and φ are the zenith and relative azimuthal angles of observation direction; Z_t is the top altitude of snow layer and

$$W_r(z, \lambda, \Omega) = \frac{\delta R(\lambda, \Omega)}{\delta r_e(z)}, \quad (2)$$

495 is the functional derivative of the function $R(\lambda, \Omega)$ with respect to the function $r_e(z)$ which is also called weighting function (Rozanov et al., 2007). The weighting function was calculated using a numerically efficient forward-adjoint approach (Rozanov, 2006; Rozanov and Rozanov, 2007) implemented in the SCIATRAN model. Here, it is assumed that properties of snow do not change in the horizontal plane and within snow layer there is no additional absorber such as soot, dust or other pollutants. We note that the weighting function
500 includes the contribution of variations not only by the scattering and extinction coefficients but also by the phase function.

Although the linear relationship given by Eq. (1) can be used to retrieve the vertical profile of the effective radius within the snow layer in a way similar to that used to the morphology of water droplets (Kokhanovsky and Rozanov, 2012), we restrict ourselves to the assumption of independent of the altitude r_e . Introducing the
505 weighting function for the absolute variation of the effective radius as:

$$W_r(\lambda, \Omega) = \int_0^{Z_t} W_r(z, \lambda, \Omega) dz, \quad (3)$$

we have

$$R(\lambda, \Omega) = R_0(\lambda, \Omega) + W_r(\lambda, \Omega) \delta r_e. \quad (4)$$

The resultant linear relationship is a basic equation to formulate inverse problem with respect to the parameter
510 r_e using measurements of spectral reflectance.

For practical applications Eq. (4) should be rewritten in the vector-matrix form as follows:

$$Y - Y_0 = K(X - X_0). \quad (5)$$

The components of vectors Y and Y_0 are the measured and simulated reflectance at discrete number of observation directions Ω_j and wavelengths λ_i , the elements of matrix K are weighting functions $W_r(\lambda_i, \Omega_j)$, $X = [r_e]$ is the state vector, $X_0 = [r_e]$ is the a priori state vector. We note that in the case under consideration, the matrix K and state vector X are represented by the column vector and scalar, respectively.

Assuming that the number of discrete observation directions Ω_j and wavelengths λ_i is larger than the dimensions of the state vector, the solution of Eq. (5) is obtained by minimizing the following cost function:

$$\Delta = \|Y - Y_0 - K(X - X_0)\|^2, \quad (6)$$

which describes the root-mean-square deviation between measured and simulated snow reflectance.

Owing to the linear relationship given by Eq. (5) the minimization problem formulated above can be solved analytically:

$$X = X_0 + (K^T K)^{-1} K^T (Y - Y_0). \quad (7)$$

In deriving Eq. (7) we have neglected the linearization error which can be significant if X_0 is far from X . To mitigate the impact of linearization error we solve minimization problem given by Eq. (6) iteratively. In particular instead of Eq. (7) is used

$$X_n = X_{n-1} + (K_{n-1}^T K_{n-1})^{-1} K_{n-1}^T (Y - Y_{n-1}), \quad (8)$$

Where $n=1, 2, \dots$ is the iteration number, K_{n-1} and Y_{n-1} are the matrix of weighting functions and reflectance vector calculated using the state vector X_{n-1} . The iteration process is finished if the difference between X_n and X_{n-1} is smaller than a preselected criteria.

The calculation of weighting functions and reflectance at flight altitude is performed at each iteration step using the radiative transfer model SCIATRAN (Rozaov et al., 2014). In SCIATRAN weighting functions are calculated employing a very efficient forward-adjoint technique, which is based on the joint solution of the linearized forward and adjoint radiative transfer equations (Rozaov 2006; Rozaov and Rozaov 2007 and references therein). This enables the TOA reflectance and required weighting function to be calculated simultaneously.

Acknowledgement

We gratefully acknowledge the funding by the Deutsche Forschungsgemeinschaft (DFG, German Research Foundation) – Project Number 268020496 – TRR 172, for SJ within the Transregional Collaborative Research Center “Arctic Amplification: Climate Relevant Atmospheric and Surface Processes, and Feedback Mechanisms (AC)3”.

Data availability. CAR and AERONET data are publicly available:

CAR: https://acdisc.gesdisc.eosdis.nasa.gov/data/CAR/CAR_ARCTAS_LIC.1/ (last access: February 2020);

AERONET: <https://aeronet.gsfc.nasa.gov/> (last access: February 2020);

545 The SCIATRAN software package is available at: <http://www.iup.uni-bremen.de/sciatran/>.

We received ozone total column data from Mark Weber (weber@uni-bremen.de).

Author contributions. SJ processed CAR data and simulated reflectance using SCIATRAN, performed the analyses for snow grain shape and size retrieval, compared the results of simulation and observation, prepared the manuscript. VVR supervised the research project (as the scientific contact of SCIATRAN) especially the simulation part, provided the snow grain shape and size retrieval algorithm, contributed to the writing and revision of the manuscript. CKG provided CAR data and contributed to the writing of paper. MV and JPB contributed to the writing of paper and general discussions.

Competing interests. The authors declare that they have no conflict of interest.

References

- 555 Aoki, Te., Aoki, Ta., Fukabori, M., and Uchiyama, A.: Numerical simulation of the atmospheric effects on snow albedo with a multiple scattering radiative transfer model for the atmosphere-snow system, *J. Meteorol. Soc. Jpn.*, 77, 595–614, https://doi.org/10.2151/jmsj1965.77.2_595, 1999.
- Arnold, G. T., Tsay, S.-C., King, M. D., Li, J. Y., Soulen, P. F.: Airborne spectral measurements of surface-atmosphere anisotropy for arctic sea ice and tundra, *Int. J. Remote Sens.*, 23(18), 3763–3781, <https://doi.org/10.1080/01431160110117373>, 2002.
- 560 Arrhenius, S.: On the influence of carbonic acid in the air upon the temperature of the ground. *Mag. J. Sci.*, London, Edinburgh, Dublin Phil, 41, 237-276, 1896.

- Bailey, M. and Hallett, J.: Growth rates and habits of ice crystals between -20C and -70C, *J. Atmos. Sci.*, 61, 514–544, [https://doi.org/10.1175/1520-0469\(2004\)061<0514:GRAHOI>2.0.CO;2](https://doi.org/10.1175/1520-0469(2004)061<0514:GRAHOI>2.0.CO;2), 2004.
- 565 Barkstrom, B.: Some Effects of Multiple Scattering on the Distribution of Solar Radiation in Snow and Ice, *J. Glaciol.*, 11(63), 357-368, <https://doi.org/10.3189/S0022143000022334>, 1972.
- Baum, B., Yang, P., J. Heymsfield, A., Bansemer, A., H. Cole, B., Merrelli, A., Schmitt, C., Wang, C.: Ice cloud single-scattering property models with the full phase matrix at wavelengths from 0.2 to 100 μm , *J. Quant. Spectrosc. Ra.*, 146, 123-139, <https://doi.org/10.1016/j.jqsrt.2014.02.029>, 2014.
- 570 Cohen, J., Screen, J. A., Furtado, J., C., Barlow, M., Whittleston, D., Coumou, D., Francis, J., Dethloff, K., Entekhabi, D., Overland, J., Jones, J.: Recent Arctic amplification and extreme mid-latitude weather, *Nat. Geosci.*, 7, 627–637, <https://doi.org/10.1038/ngeo2234>, 2014.
- Curry, J. A., Schramm, J. L., Ebert, E. E.: Sea Ice-Albedo Climate Feedback Mechanism, *J. Climate*, 8, 240–247, [https://doi.org/10.1175/1520-0442\(1995\)008<0240:SIACFM>2.0.CO;2](https://doi.org/10.1175/1520-0442(1995)008<0240:SIACFM>2.0.CO;2), 1995.
- 575 Dunkle, R.V. and Bevans, J.T.: An approximate analysis of the solar reflectnce and transmittance of a snow cover, *J. Meteorol.*, 13, 212–216, [https://doi.org/10.1175/15200469\(1956\)013<0212:AAAOTS>2.0.CO;2](https://doi.org/10.1175/15200469(1956)013<0212:AAAOTS>2.0.CO;2), 1956.
- Gatebe, C. K., King, M. D., Lyapustin, A. I., Arnold, G. T., Redemann, J.: Airborne spectral measurements of ocean directional reflectance, *J. Atmos. Sci.*, 62, 1072–1092, <https://doi.org/10.1175/JAS3386.1>, 2005.
- 580 Gatebe, C. & King, M.: Airborne spectral BRDF of various surface types (ocean, vegetation, snow, desert, wetlands, cloud decks, smoke layers) for remote sensing applications, *Remote Sens. Environ.*, 179, 131-148. [10.1016/j.rse.2016.03.029](https://doi.org/10.1016/j.rse.2016.03.029), 2016.
- Hudson, S. R., Warren, S. G., Brandt, R. E., Grenfell, T. C., Six, D.: Spectral bidirectional reflectance of Antarctic snow: measurements and parameterization, *J. Geophys. Res.*, 111, D18106, <https://doi.org/10.1029/2006JD007290>, 2006.
- 585 Hudson, S. R. and Warren, S. G.: An explanation for the effect of clouds over snow on the top-of atmosphere bidirectional reflectance, *J. Geophys. Res.*, 112, D19202, <https://doi.org/10.1029/2007JD008541>, 2007.
- Istomina, L. G., von Hoyningen-Huene, W., Kokhanovsky, A. A., and Burrows, J. P.: The detection of cloud-free snow-covered areas using AATSR measurements, *Atmos. Meas. Tech.*, 3, 1005–1017, <https://doi.org/10.5194/amt-3-1005-2010>, 2010.
- 590 Istomina, L.: Retrieval of aerosol optical thickness over snow and ice surfaces in the Arctic using Advanced Along Track Scanning Radiometer, PhD thesis, University of Bremen, Bremen, Germany, 2012.

- Jafariserajehlou, S., Mei, L., Vountas, M., Rozanov, V., Burrows, J. P. and Hollmann, R.: A cloud identification algorithm over the Arctic for use with AATSR-SLSTR measurements, *Atmos. Meas. Tech.*, 12, 1059-1076, <https://doi.org/10.5194/amt-12-1059-2019>, 2019.
- 595
- Jin, Z., Charlock, T. P., Yang, P., Xie, Y., Miller, W.: Snow optical properties for different particle shapes with application to snow grain size retrieval and MODIS/CERES radiance comparison over Antarctica, *Remote Sens. Environ.*, 112, 3563–3581, <https://doi.org/10.1016/j.rse.2008.04.011>, 2008.
- Kim, B. M., Hong, J. Y., Jun, S. Y., Zhang, X., Kwon, H., Kim, S. J., Kim, J. H., Kim, S. W., Kim, H. K.: Major cause of unprecedented Arctic warming in January 2016: critical role of an Atlantic windstorm, *Sci. Rep-UK*, 7, 40051, <https://doi.org/10.1038/srep40051>, 2017.
- 600
- Kokhanovsky, A. A., and Zege, E. P.: Scattering optics of snow, *Appl. Optics.*, 43, 1589–1602. <https://doi.org/10.1364/AO.43.001589>, 2004.
- Kokhanovsky, A. A., Aoki, T., Hachikubo, A., Hori, M., and Zege, E. P.: Reflective properties of natural snow: approximate asymptotic theory versus in situ measurements, *IEEE Transactions on Geoscience and Remote Sensing*, 43, 1529-1535, doi: 10.1109/TGRS.2005.848414, 2005.
- 605
- Kokhanovsky, A. A., Budak, V. P., Cornet, C., Duan, M., Emde, C., Katsev, I. L., Klyukov, D. A., Korkin, S. V., C-Labonnote, L., Mayer, B., Min, Q., Nakajima, T., Ota, Y., Prikhach, A. S., Rozanov, V. V., Yokota, T., Zege, E. P.: Benchmark results in vector atmospheric radiative transfer, *J. Quant. Spectrosc. Ra.*, 111, 1931–46, <https://doi.org/10.1016/j.jqsrt.2010.03.005>, 2010.
- 610
- Kokhanovsky, A., Rozanov, V.V., Aoki, T., Odermatt, D., Brockmann, C., Krüger, O., Bouvet, M., Drusch, M., Hori, M.: Sizing snow grains using backscattered solar light, *Int. J. Remote Sens.*, 32:22, 6975-7008, <https://doi.org/10.1080/01431161.2011.560621>, 2011.
- Kokhanovsky, A. A., and Breon, F.: Validation of an Analytical Snow BRDF Model Using PARASOL Multi-Angular and Multispectral Observations, *IEEE Geosci. Remote S.*, 9, 928-932, [10.1109/LGRS.2012.2185775](https://doi.org/10.1109/LGRS.2012.2185775), 2012.
- 615
- Kokhanovsky, A. A. and Rozanov, V. V.: Droplet vertical sizing in warm clouds using passive optical measurements from a satellite, *Atmos. Meas. Tech.*, 5, 517-528, <https://doi.org/10.5194/amt-5-517-2012>, 2012.
- 620
- Leroux, C., Deuzé, J.-L., Goloub, P., Sergent, C., Fily, M.: Ground measurements of the polarized bidirectional reflectance of snow in the near-infrared spectral domain: Comparisons with model results, *J. Geophys. Res.*, 103(D16), 19721–19731, <https://doi.org/10.1029/98JD01146>, 1998.

- Leroux, C., Lenoble, J., Brogniez, G., Hovenier, J.W., De Haan, J.F.: A model for the bidirectional polarized reflectance of snow, *J. Quant. Spectrosc. Ra.*, 61, 3, 273-285, [https://doi.org/10.1016/S0022-4073\(97\)00221-5](https://doi.org/10.1016/S0022-4073(97)00221-5), 1999.
- 625
- Levy, R.C., Remer, L.A., Mattoo, S., Vermte, E. F., Kaufman, Y.J.: Second-generation operational algorithm: Retrieval of aerosol properties over land from inversion of Moderate Resolution Imaging Spectroradiometer spectral reflectance, *J. Geophys. Res.*, 112, D13211, <https://doi.org/10.1029/2006JD007811>, 2007.
- Li, S., and Zhou, X., Modelling and measuring the spectral bidirectional reflectance factor of snow-covered sea ice: An intercomparison study. *Hydrol. Process.* 18(18), 3559–3581, <https://doi.org/10.1002/hyp.5805>, 2004.
- 630
- Libbrecht, K. G.: The formation of snow crystal, *Am. Sci.*, 95, 52–59, 2007.
- Lyapustin, A., Gatebe, C. K., Kahn, R., Brandt, R., Redemann, J., Russell, P., King, M. D., Pedersen, C. A., Gerland, S., Poudyal, R., Marshak, A., Wang, Y., Schaaf, C., Hall, D., Kokhanovsky, A. A.: Analysis of snow bidirectional reflectance from ARCTAS spring-2008 campaign, *Atmos. Chem. Phys.*, 10, 4359–75, <https://doi.org/10.5194/acp-10-4359-2010>, 2010.
- 635
- Macke, A., Mueller, J., Raschke, E.: Scattering properties of atmospheric ice crystals, *J. Atmos. Sci.*, 53, 2813–25, [https://doi.org/10.1175/1520-0469\(1996\)053<2813:SSPOAI>2.0.CO;2](https://doi.org/10.1175/1520-0469(1996)053<2813:SSPOAI>2.0.CO;2), 1996.
- Middleton, W., & Mungal, A.: The luminous directional reflectance of snow, *J. Opt. Soc. Am.*, 42(8), <https://doi.org/10.1364/JOSA.42.000572>, 1952.
- 640
- Mishchenko, M. I.: Asymmetry parameters of the phase function for densely packed scattering grains, *J. Quant. Spectrosc. Ra.*, 52, 95–110, [https://doi.org/10.1016/0022-4073\(94\)90142-2](https://doi.org/10.1016/0022-4073(94)90142-2), 1994.
- Mishchenko, M. I., Dlugach, J. M., Yanovitskij, E. G., Zakharova, N. T.: Bidirectional reflectance of flat, optically thick particulate layers: an efficient radiative transfer solution and applications to snow and soil surfaces, *J. Quant. Spectrosc. Ra.*, 63, 409–432, [https://doi.org/10.1016/S0022-4073\(99\)00028-X](https://doi.org/10.1016/S0022-4073(99)00028-X), 1999.
- 645
- Mishchenko, M. I.: Directional radiometry and radiative transfer: The convoluted path from centuries-old phenomenology to physical optics, *J. Quant. Spectrosc. Ra.*, 146, 4–33, <https://doi.org/10.1016/j.jqsrt.2014.02.033>, 2014.
- Negi, H. S. and Kokhanovsky, A.: Retrieval of snow albedo and grain size using reflectance measurements in Himalayan basin, *The Cryosphere*, 5, 203-2017, [10.5194/tc-5-203-2011](https://doi.org/10.5194/tc-5-203-2011), 2011.
- 650
- Nicodemus, F. E.: Directional reflectance and emissivity of an opaque surface, *Appl. Optics.*, 4, 767–773, <https://doi.org/10.1364/AO.4.000767>, 1965.

- Nicodemus, F. E., Richmond, J. C., Hsia, J. J., Ginsberg, I. W., Limperis, T.: Geometrical considerations and nomenclature for reflectance, in: Wolff, L. B., Shafer, S. A., and Healey, G. (Eds.), *Radiometry*. Jones and Bartlett Publishers, Inc., USA, pp. 94-145, <http://dl.acm.org/citation.cfm?id=136913.136929>, 1977.
- 655 Painter, T. H., Dozier, J., Roberts, D. A., Davis, R. E., Greene, R. O.: Retrieval of subpixel snow-covered area and grain size from imaging spectrometer data, *Remote Sens. Environ.*, 85, 64–77, [https://doi.org/10.1016/S0034-4257\(02\)00187-6](https://doi.org/10.1016/S0034-4257(02)00187-6), 2003.
- Pohl, C., Rozanov, V., Wendisch, M., Spreen, G., Heygster, G.: Impact of near-field effect on bidirectional reflectance factor and albedo of snow calculated by a phenomenological radiative transfer model, *J. Quant. Spectrosc. Ra.*, <https://doi.org/10.1016/j.jqsrt.2019.106704>, 2020.
- 660 Pohl, C., Rozanov, V. V., Mei, L., Burrows, J. P., Heygster, G., Spreen, G.: Implementation of an extensive ice crystal single-scattering property database in the radiative transfer model SCIATRAN, *J. Quant. Spectrosc. Ra.*, 253, <https://doi.org/10.1016/j.jqsrt.2020.107118>, 2020.
- Quinn, P. K., Miller, T. L., Bates, T. S., Ogren, J. A., Andrews, E., & Shaw, G. E.: A 3-year record of simultaneously measured aerosol chemical and optical properties at Barrow, Alaska, *J. Geophys. Res., Atmos.*, 107(D11), AAC 8-1–AAC 8-15, 2002.
- 665 Rozanov, V. V., Buchwitz, M., Eichmann, K. U., de Beek, R., Burrows, J. P.: SCIATRAN – a new radiative transfer model for geophysical applications in the 240–2400 nm spectral region: the pseudo-spherical version, *Adv. Space. Res.*, 29 (11), 1831–1835, [https://doi.org/10.1016/S0273-1177\(02\)00095-9](https://doi.org/10.1016/S0273-1177(02)00095-9), 2002.
- 670 Rozanov, V. V.: Adjoint radiative transfer equation and inverse problems, in: Kokhanovsky, A. A. (Eds.), *Light Scattering Reviews: Single and Multiple Light Scattering*. Springer Berlin Heidelberg, Berlin, Heidelberg, pp. 339-392, https://doi.org/10.1007/3-540-37672-0_8, 2006.
- Rozanov, V.V. and Rozanov, A.V.: Relationship between different approaches to derive weighting functions related to atmospheric remote sensing problems, *J. Quant. Spectrosc. Ra.*, 105(2), 217-242, <https://doi.org/10.1016/j.jqsrt.2006.12.006>, 2007.
- 675 Rozanov, V. V., Rozanov, A. V., Kokhanovsky, A. A.: Derivatives of the radiation field and their application to the solution of inverse problems, in: Kokhanovsky, A. A. (Eds.), *Light Scattering Reviews 2: Remote Sensing and Inverse Problems*. Springer Berlin Heidelberg, Berlin, Heidelberg, pp. 205-265, https://doi.org/10.1007/978-3-540-68435-0_6, 2007.
- 680 Rozanov, V.V., Rozanov, A.V., Kokhanovsky, A.A., Burrows, J. P.: Radiative transfer through terrestrial atmosphere and ocean: Software package SCIATRAN, *J. Quant. Spectrosc. Ra.*, 133. 13-71, <https://doi.org/10.1016/j.jqsrt.2013.07.004>, 2014.

- Serreze, M. C., and Barry, R. C.: Processes and impacts of Arctic amplification: A research synthesis, *Global Planet. Change*, 77, 85–96, [doi:10.1016/j.gloplacha.2011.03.004](https://doi.org/10.1016/j.gloplacha.2011.03.004), 2011.
- 685 Schaeppman-Strub, G., Schaeppman, M. E., Painter, T. H., Dangel, S., Martonchik, J. V.: Reflectance quantities in optical remote sensing-definitions and case studies, *Remote Sens. Environ.*, 103, 27–42, <https://doi.org/10.1016/j.rs6e.2006.03.002>, 2006.
- Schneider, S.H. and Dickinson, R. E., Climate modeling, *Rev. Geophys.*, 12, 447–493, <https://doi.org/10.1029/RG012i003p00447>, 1974.
- 690 Shultz, M. J.: Crystal growth in ice and snow, *Phys. Today.*, 71, 35–39, <https://doi.org/10.1063/PT.3.3844>, 2018.
- Sinnhuber, B. M., Sheode, N., Sinnhuber, M., Chipperfield, M. P., Feng, W.: The contribution of anthropogenic bromine emissions to past stratospheric ozone trends: a modelling study, *Atmos. Chem. Phys.*, 9, 2863–71, <https://doi.org/10.5194/acp-9-2863-2009>, 2009.
- 695 Slater, B., and Michaelides, A.: Surface premelting of water ice. *Nature Reviews Chemistry*, 3:3, 172–188, <https://doi.org/10.1038/s41570-019-0080-8>, 2019.
- Soulen, P. F., King, M. D., Tsay, S. C., Arnold, G. T., Li, J. Y.: Airborne spectral measurements of surface-atmosphere anisotropy during the SCAR-A, Kuwait oil fire, and TARFOX experiments, *J. Geophys. Res.*, 105, 10203–10218, <https://doi.org/10.1029/1999JD901115>, 2000.
- 700 Udisti, R., Traversi, R., Becagli, S., Tomasi, C., Mazzola, M., Lupi, A., and Quinn, P. K. : Arctic Aerosols in: Physics and Chemistry of the Arctic Atmosphere, edited by: Kokhanovsky, A. A., Tomasi, C., Springer Nature Switzerland AG, Cham, Switzerland, 2020.
- Warren, S. G.: Optical Properties of Snow, *Rev. Geophys. Space Ge.*, 20, 67–89, <https://doi.org/10.1029/RG020i001p00067>, 1982.
- 705 Warren, S. G., Brandt, R. E., Hinton P. O. R.: Effect of surface roughness on bidirectional reflectance of Antarctic snow, *J. Geophys. Res.*, 103:25789–807, <https://doi.org/10.1029/98JE01898>, 1998.
- Weber, M., Coldewey-Egbers, M., Fioletov, V. E., Frith, S. M., Wild, J. D., Burrows, J. P., Long, C. S., Loyola, D.: Total ozone trends from 1979 to 2016 derived from five merged observational datasets – the emergence into ozone recovery, *Atmos. Chem. Phys.*, 18, 2097–2117, <https://doi.org/10.5194/acp-18-2097-2018>, 2018.
- 710 Wendisch, M., Brückner, M., Burrows, J. P., Crewell, S., Dethloff, K., Ebell, K., Lüpkes, C., Macke, A., Notholt, J., Quaas, J., Rinke, A., and Tegen, I.: Understanding causes and effects of rapid warming in the Arctic, *Eos*, 98, 22–26, <https://doi.org/10.1029/2017EO064803>, 2017.
- Wendisch, M., Macke, A., Ehrlich, A., Lüpkes, C., Mech, M., Chechin, D., Dethloff, K., Barrientos, C., Bozem, H., Brückner, M., Clemen, H. C., Crewell, S., Donth, T., Dupuy, R., Dusny, C, Ebell, K., Egerer, U.,

- 715 Engelmann, R., Engler, C., Eppers, O., Gehrman, M., Gong, X., Gottschalk, M., Gourbeyre, C., Griesche, H., Hartmann, J., Hartmann, M., Heinold, B., Herber, A., Herrmann, H., Heygster, G., Hoor, P., Jafariserajehlou, S., Jäkel, E., Järvinen, E., Jourdan, O., Kästner, U., Kecorius, S., Knudsen, E.M., Köllner, F., Kretzschmar, J., Lelli, L., Leroy, D., Maturilli, M., Mei, L., Mertes, S., Mioche, G., Neuber, R., Nicolaus, M., Nomokonova, T., Notholt, J., Palm, M., van Pinxteren, M., Quaas, J., Richter, P., Ruiz-Donoso, E.,
- 720 Schäfer, M., Schmieder, K., Schnaiter, M., Schneider, J., Schwarzenböck, A., Seifert, P., Shupe, M.D., Siebert, H., Spreen, G., Stapf, J., Stratmann, F., Vogl, T., Welti, A., Wex, H., Wiedensohler, A., Zanatta, M., Zeppenfeld, S.: The Arctic Cloud Puzzle: Using ACLOUD/PASCAL Multi-Platform Observations to Unravel the Role of Clouds and Aerosol Particles in Arctic Amplification, *Bull. Amer. Meteor. Soc.*, 100 (5), 841–871, [doi:10.1175/BAMS-D-18-0072.1](https://doi.org/10.1175/BAMS-D-18-0072.1), 2019.
- 725 Wiscombe, W. J. and Warren, S. G.: A model for the spectral albedo of snow. I. Pure snow, *J. Atmos. Sci.*, 37, 2712–2733, [https://doi.org/10.1175/1520-0469\(1980\)037<2712:AMFTSA>2.0.CO;2](https://doi.org/10.1175/1520-0469(1980)037<2712:AMFTSA>2.0.CO;2), 1980.
- Yang, P. and Liou, K. N.: Single-scattering properties of complex ice crystals in terrestrial atmosphere, *Contr. Atmos. Phys.*, 71, 223–248, 1998.
- Yang, P., Baum, B. A., Heymsfield, A. J., Hu, Y. X., Huang, H. L., Tsay, S. C., Ackerman, S.: Single-scattering
- 730 properties of droxtals, *J. Quant. Spectrosc. Ra.*, 79–80, 1159–1169, [https://doi.org/10.1016/S0022-4073\(02\)00347-3](https://doi.org/10.1016/S0022-4073(02)00347-3), 2003.
- Yang, P., Bi, L., Baum, B. A., Liou, K., Kattawar, G. W., Mishchenko, M. I., Cole, B.: Spectrally Consistent Scattering, Absorption, and Polarization Properties of Atmospheric Ice Crystals at Wavelengths from 0.2 to 100 μm , *J. Atmos. Sci.*, 70, 330–347, <https://doi.org/10.1175/JAS-D-12-039.1>, 2013.
- 735 Zhuravleva, T. B., Kokhanovsky, A. A.: Influence of surface roughness on the reflective properties of snow, *J. Quant. Spectrosc. Ra.*, 112(8), 1353-1368, <https://doi.org/10.1016/j.jqsrt.2011.01.004>, 2011.

Table1. Summary of the CAR, AERONET aerosol optical thickness (transferred from 0.5 to 0.55 μm) and WFDOS ozone data used in this study.

Dataset number	1	2	3	4
Date	7 th April 2008	7 th April 2008	7 th April 2008	15 th April 2008
Location	Elson-Lagoon	Elson-Lagoon	Elson-Lagoon	Elson-Lagoon
Flight altitude	206 m	647 m	1700 m	181 m
SZA (θ_0)	70.23°	69.11°	67.78°	62.11°
AOT (τ 0.55 μm)	0.11	0.11	0.11	0.15
Total ozone column	416 DU	416 DU	416 DU	463.4 DU

Table2. Summary of CAR wavelengths and bandwidth

Channel number	Central wavelengths	Bandwidth
	in μm	in nm
1	0.480	21
2	0.687	26
3	0.340	9
4	0.381	6
5	0.870	10
6	1.028	4
7	0.609	9
8	1.275	24
9	1.554	33
10	1.644	46
11	1.713	46
12	2.116	43
13	2.203	43
14	2.324	48

740 **Table 3.** Retrieval of physical characteristics of ice crystals with different shape in the case of most roughened habits. Underlined numbers indicate minimum RMSE.

Ice crystal habit	Asymmetry parameter		Retrieved effective radius (μm)		Old snow		Fresh snow	
	Old snow Fresh snow		Old snow Fresh snow		Bias (%) RMSE (%)		Bias (%) RMSE (%)	
Fractal	0.825	0.827	69.37	76.06	3.50	9.75	13.16	14.69
Droxtal	0.856	0.863	94.48	106.95	0.87	25.54	10.10	34.14
Column	0.873	0.877	74.71	80.49	2.17	7.32	12.36	15.72
Hollow column	0.884	0.888	67.32	72.85	2.80	11.15	13.66	15.14
Aggregate of 8 columns	0.844	0.849	98.83	107.62	2.79	<u>6.97</u>	11.85	18.27
Plate	0.923	0.942	38.93	61.44	-0.44	21.47	11.68	16.99
Aggregate of 5 plates	0.874	0.877	78.02	83.41	1.82	10.34	11.23	<u>12.85</u>
Aggregate of 10 plates	0.893	0.893	65.36	69.28	2.34	13.91	11.52	13.16
Hollow-bullet rosette	0.887	0.889	67.01	73.28	2.16	9.99	12.71	15.16

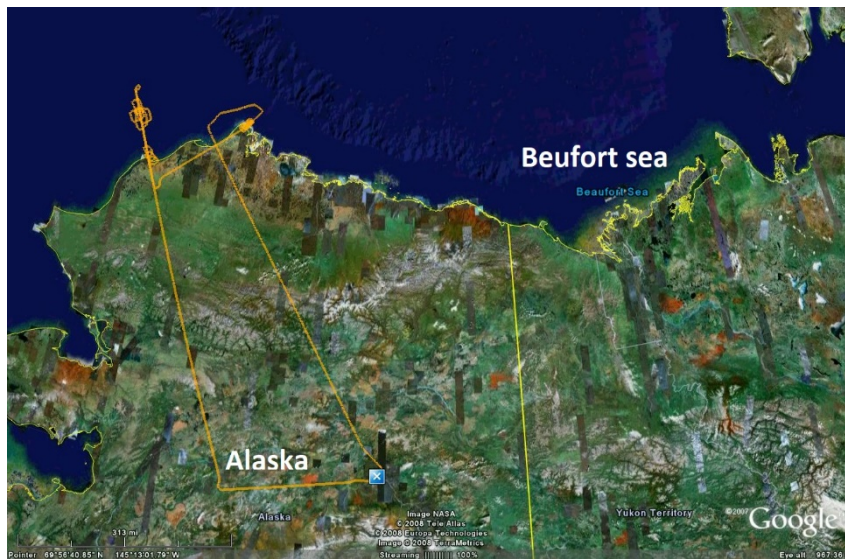
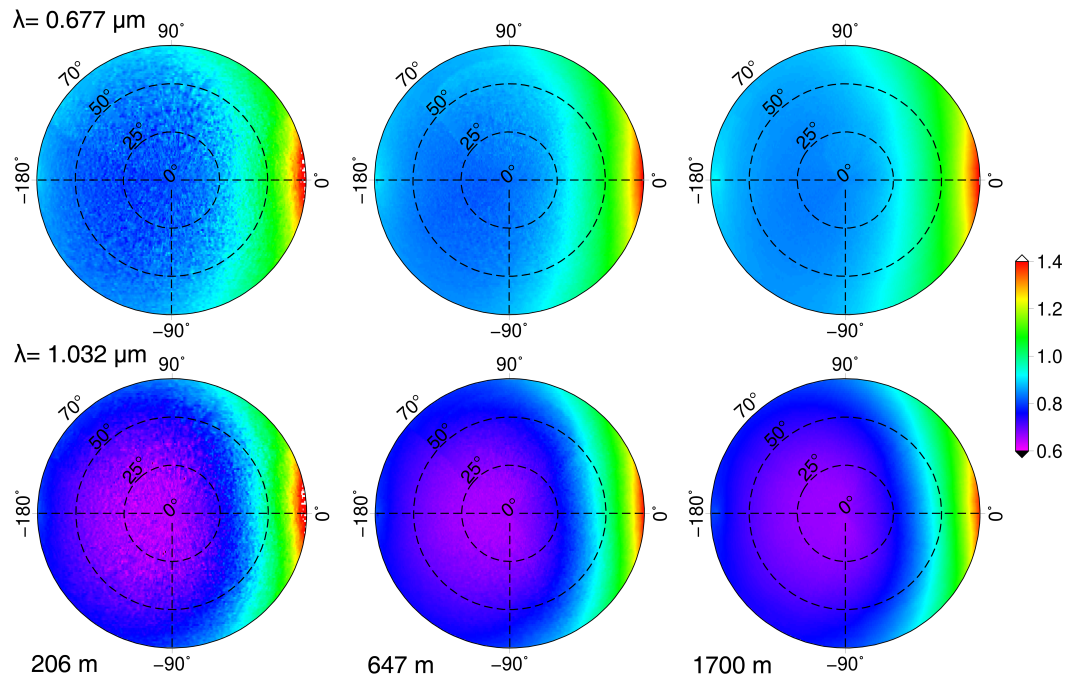
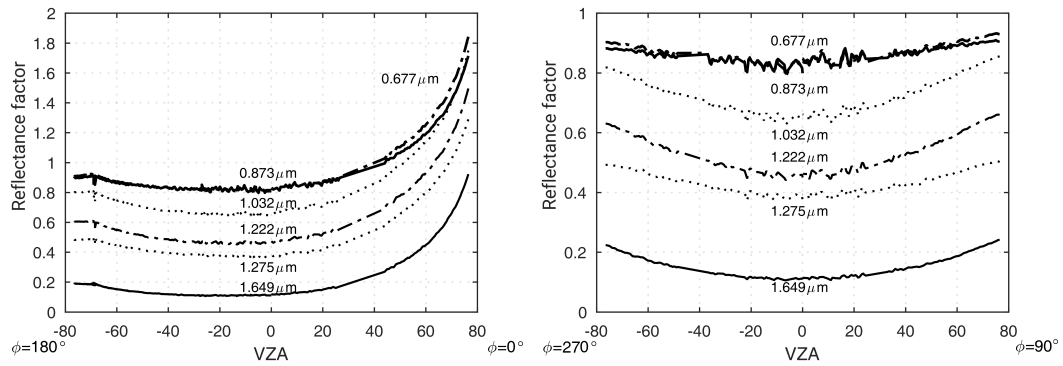


Figure 1: Flight track of P-3B airplane carrying CAR on 07.04.2008 during ARCTAS campaign (Credit: NASA)



745 **Figure 2:** Angular distribution of reflectance factor in the snow-atmosphere system derived from CAR measurements on 7th of April 2008, at Elson Lagoon (71.3° N, 156.4° W): Upper panel at 0.677 μm wavelength and 3 flight altitudes: 206, 647 and 1700 m, respectively; lower panel at 1.032 μm wavelength and at the same flight altitudes. The principal plane is the horizontal line ($\varphi = 0^\circ$ and 180°), viewing zenith angle is shown as the radius of polar plots from 0° (nadir) to 70° , solar zenith angle is 70.23° , 69.11° and 67.78° for flight altitude of 206, 647 and 1700 m respectively.



750 **Figure 3:** Angular distribution of reflectance factor in the snow-atmosphere system, derived from measurements by CAR at 647 m flight altitude and six wavelengths: 0.677 μm , 0.873 μm , 1.032 μm , 1.222 μm , 1.275 μm and 1.649 μm , on 7th of April 2008, at Elson Lagoon (71.3° N, 156.4° W); left panel: in the principal plane ($\phi = 0^\circ$ and 180°) and right: cross plane ($\phi = 90^\circ$ and 270°).

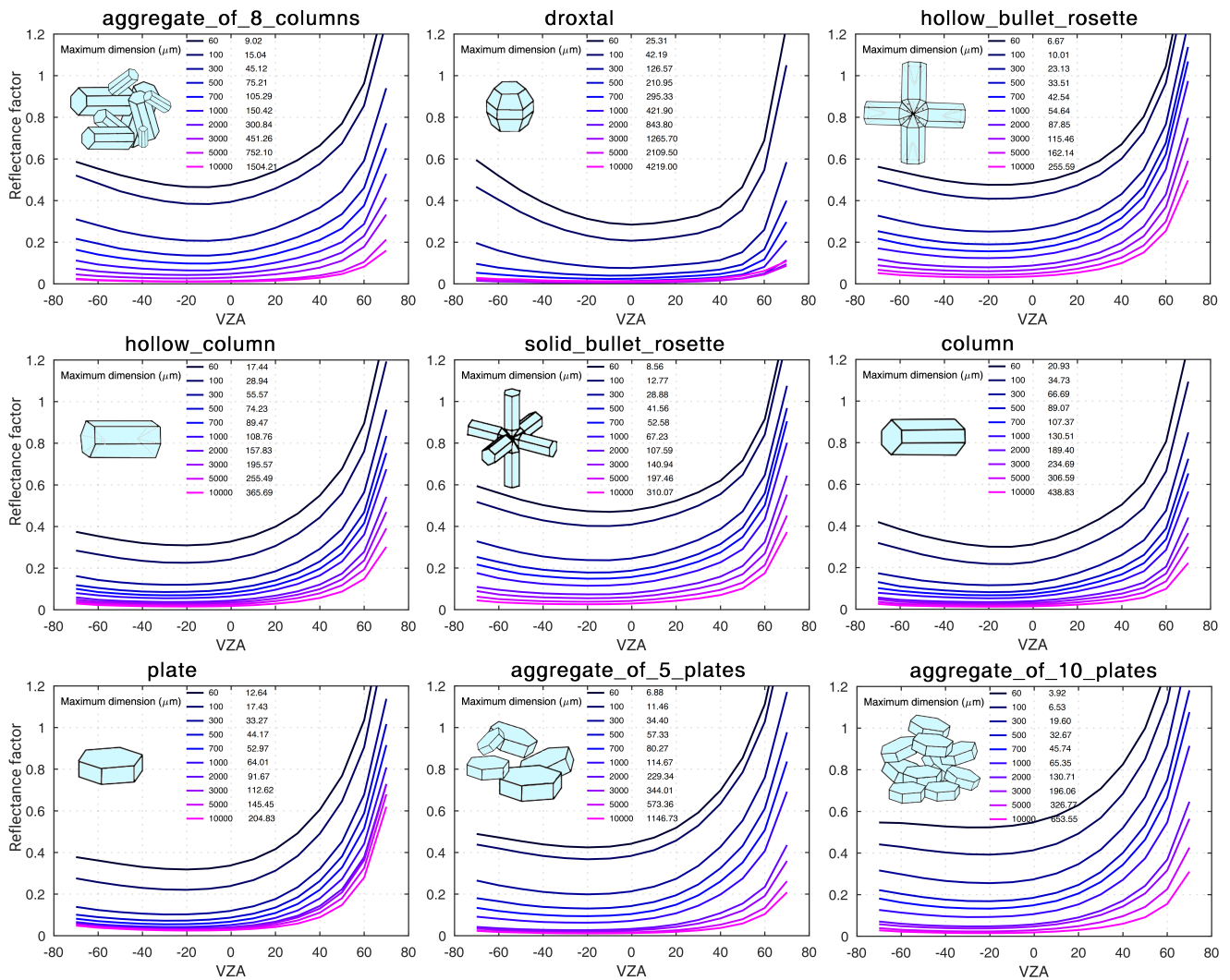


Figure 4: The change of reflectance factor values in principal plane ($\varphi = 0^\circ$ and 180°) with size and shape of ice crystals at the wavelength of $1.649 \mu\text{m}$, left column in each figure shows the maximum length of ice crystal and right column is its equivalent effective radius.

755

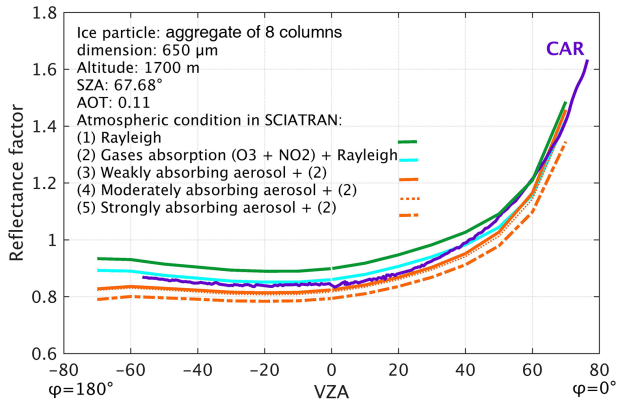
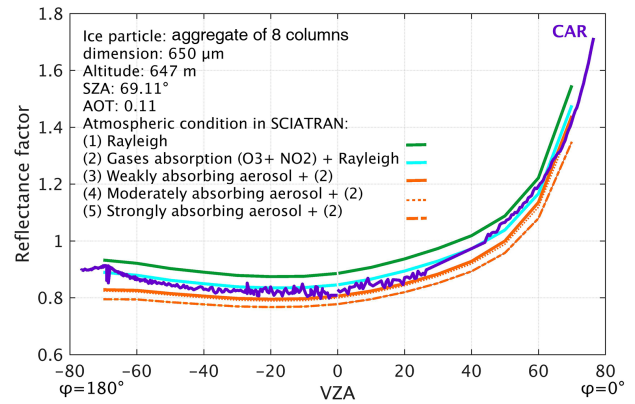
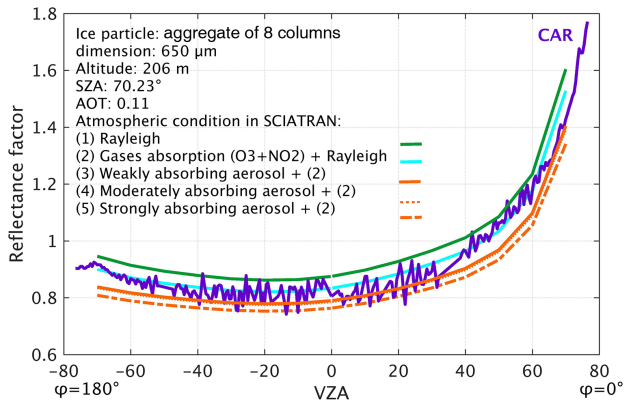


Figure 5: Measured and simulated reflectance factor at 0.677 μm versus VZA in the principal plane ($\phi = 0^\circ$ and 180°) at three different flight altitudes. Upper left, upper right and the lower left panel represent results at 206, 647 and 1700 m flight altitude respectively. The green lines indicate simulated reflectance assuming Rayleigh scattering (case i); the blue line shows reflectance for case ii (as case i including absorption of O₃ and NO₂, the orange lines show the reflectance for case iii (as case ii but adding aerosol with an AOT of 0.11 for three types of aerosol: i) weakly absorbing, ii) moderately absorbing and iii) strongly absorbing).

760

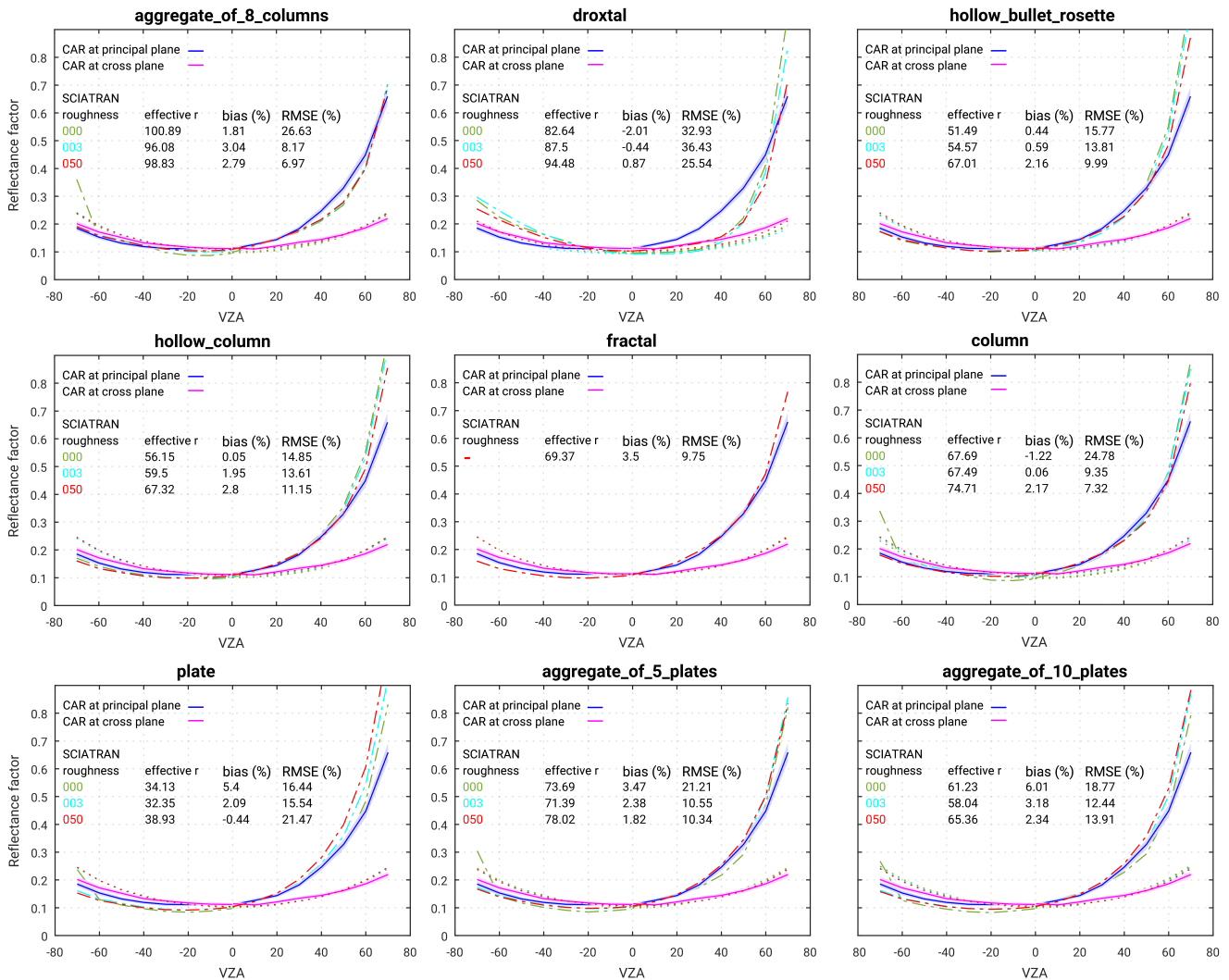


Figure 6: Comparison of measured and simulated reflectance factor. Measurements were performed by the CAR instrument over old snow at 647 m flight altitude on the 7th of April 2008 at 1.649 μm . The uncertainty in CAR measurements is indicated by envelope. SCIATRAN simulations in the principal and cross plane given by the dashed-dotted and dotted lines respectively by different colors: green, blue and red present smooth, moderately roughened and severely roughened crystal surface. Positive and negative VZAs correspond to azimuthal angles $\phi = 0^\circ$ and 180° for principal plane and $\phi = 90^\circ$ and 270° for perpendicular plane respectively.

765

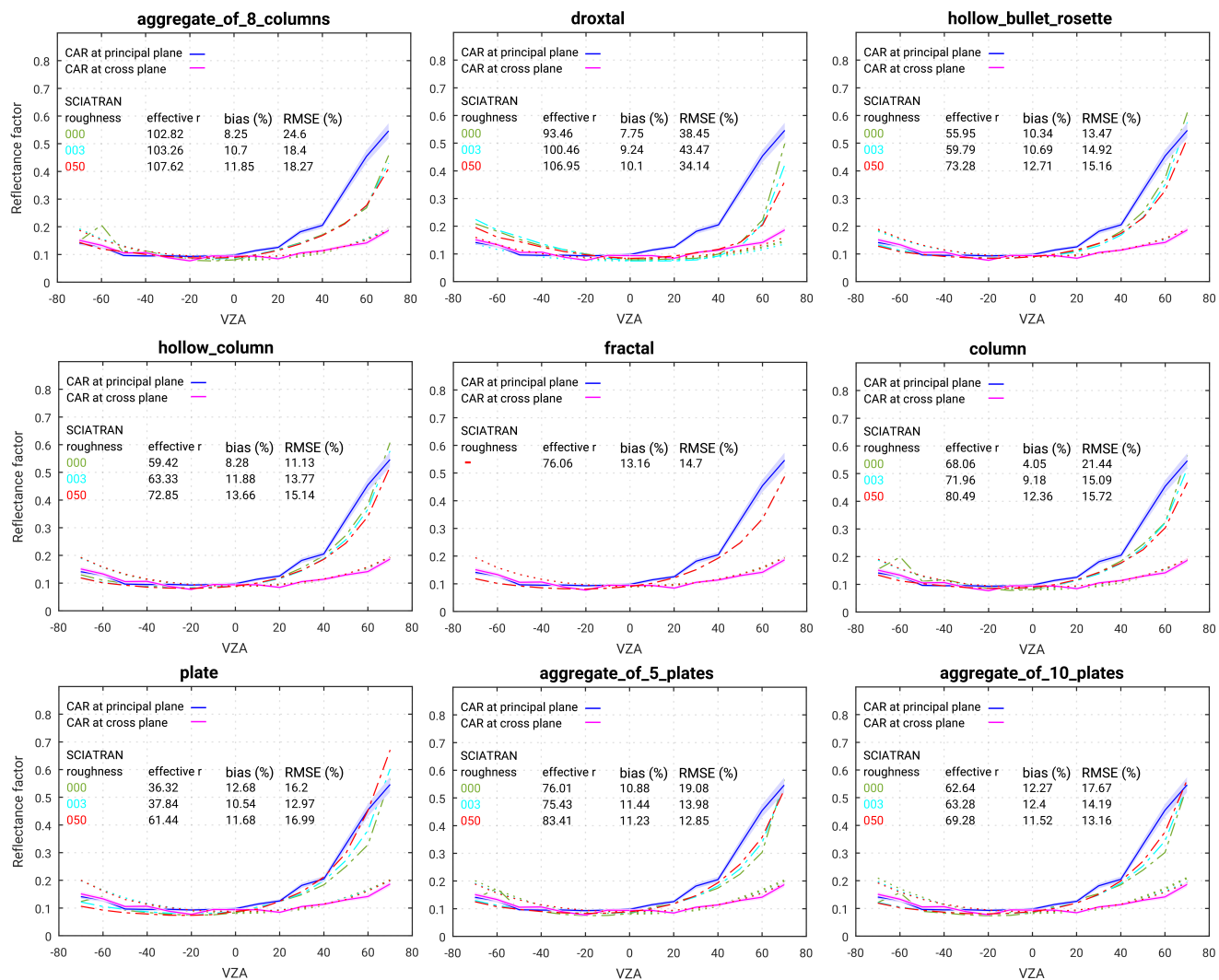
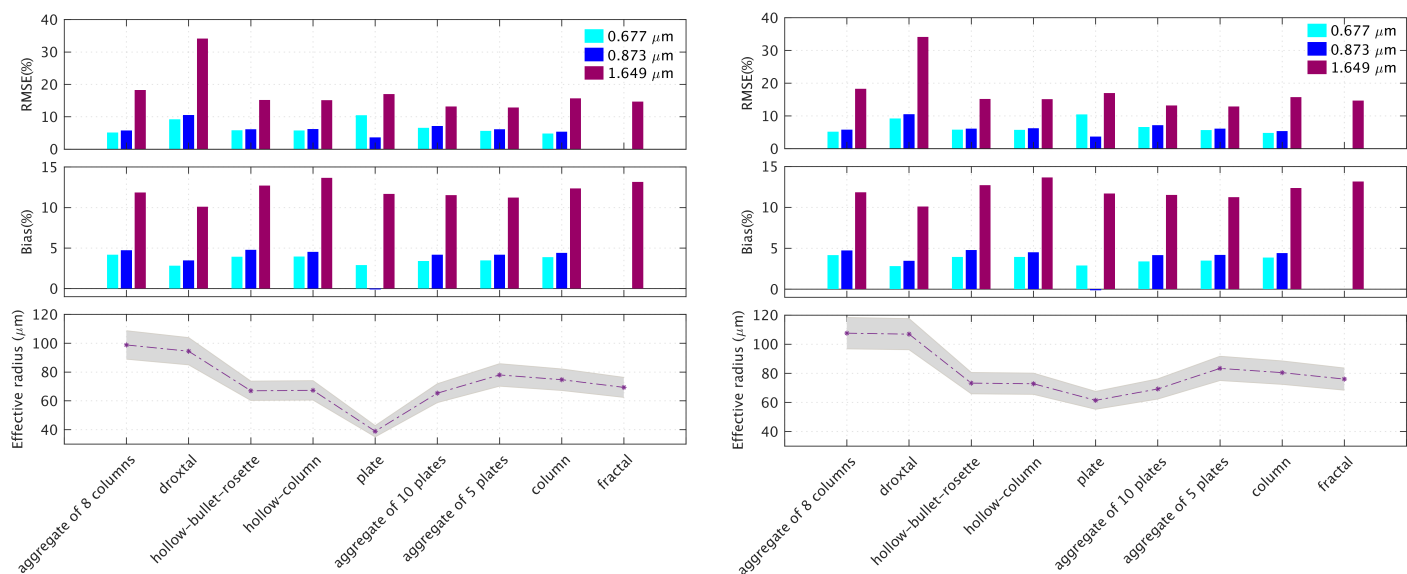


Figure 7: The same as Fig. 6 but the measurements by the CAR instrument were performed on the 15th April at 181 m flight altitude over fresh snow.



770 **Figure 8:** Comparison of snow grain size retrieval and best fit of reflectance at three wavelengths: 0.677, 0.873 and 1.649 μm , left panel: old snow case and right panel: fresh snow case. Effective radius is retrieved at 1.649 μm and grey envelope shows the uncertainty in the retrieved effective radius.

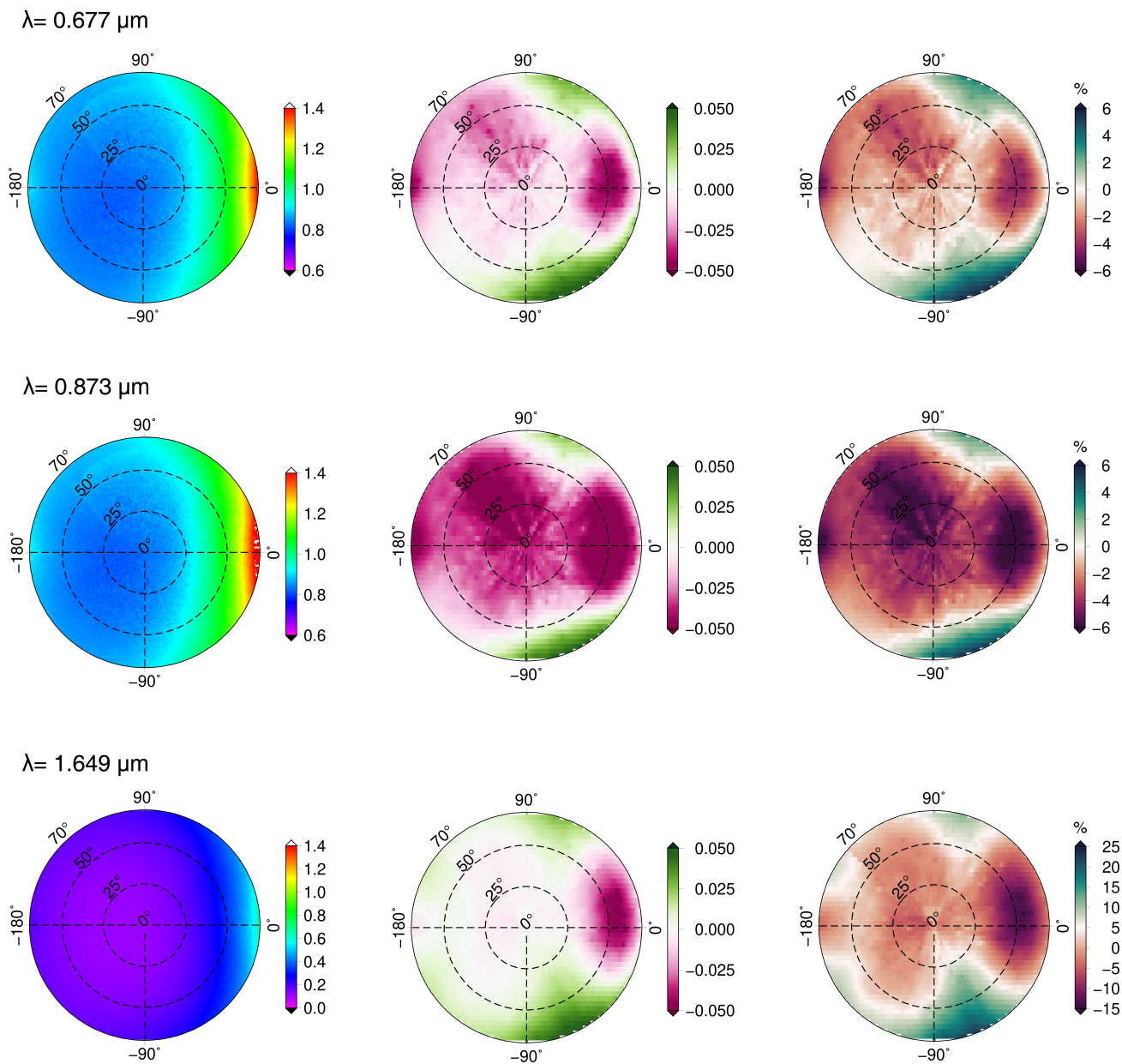


Figure 9: Left column shows reflectance factor at three wavelengths: 0.677, 0.873 and 1.649 μm from the CAR measurements acquired on 7th of April 2008, at Barrow/Utqiagvik Alaska at an altitude of 647 m; The middle column depicts the absolute difference between simulation and measurement: $(R_{\text{SCIATRAN}} - R_{\text{CAR}})$; The right column shows the relative difference in (%).

775

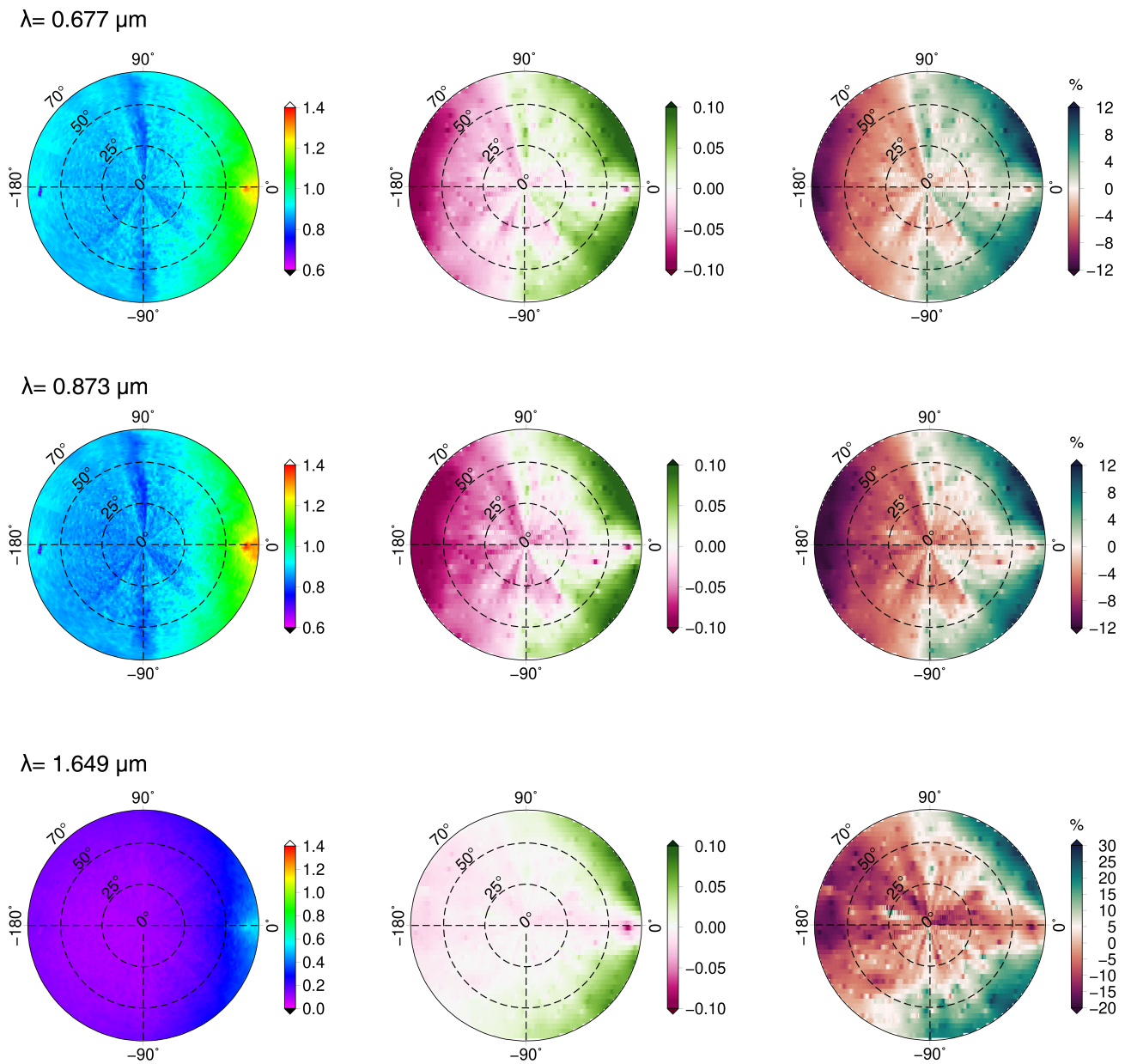
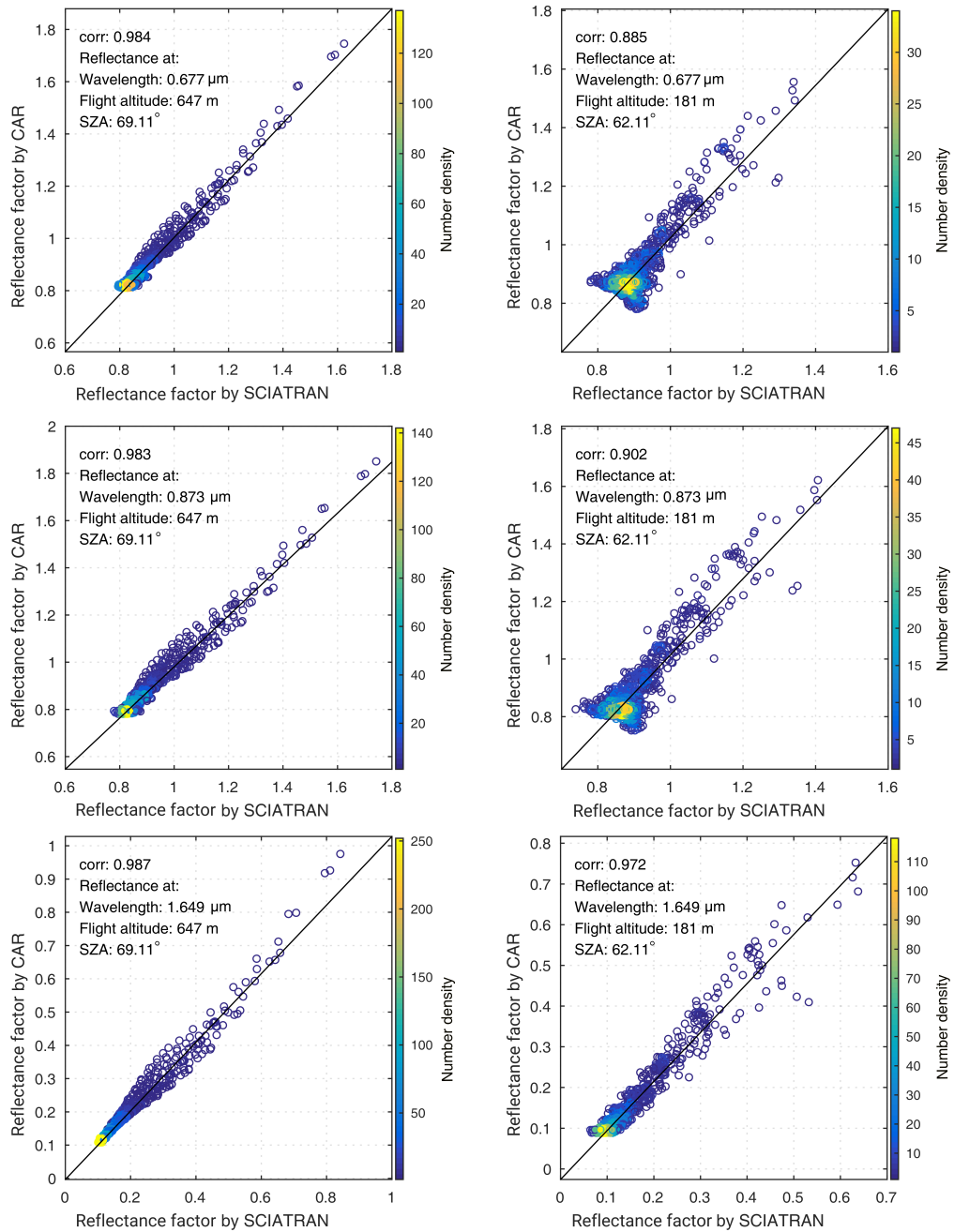


Figure 10: The same as Fig. 9 but the measurements by CAR instrument were performed on 15th April 2008 at 181 m flight altitude over fresh snow.



780 **Figure 11:** The scatter plot with corresponding Pearson correlation coefficient of reflectance factor measured by CAR and simulated by SCIATRAN; left column shows the results for old snow, right column: fresh snow. Here the color bar represents number density of pixels.